

STABLE AND UNSTABLE MOLECULES UNDER SUPERCRITICAL
AND CRYOGENIC CONDITIONS

By

TROY D. HALVORSEN

A DISSERTATION PRESENTED TO THE GRADUATE SCHOOL
OF THE UNIVERSITY OF FLORIDA IN PARTIAL FULFILLMENT
OF THE REQUIREMENTS FOR THE DEGREE OF
DOCTOR OF PHILOSOPHY

UNIVERSITY OF FLORIDA

1998

ACKNOWLEDGEMENTS

The author wishes to thank first and foremost his family whose love and support have fostered his growth as an individual and has propelled him to this position in his life. His mother (Susan) who personally sacrificed and was unwilling to let the author accept anything but the best. His dad (Joe) who first introduced the author to academia and has “gently” guided his path towards higher education. The author does not believe that his dad would have ever believed in his wildest dreams that he would eventually accept an assistant professorship at Truman State University. When his dad dropped him off at Illinois State University in the fall of 1986 to begin his undergraduate career as a chemistry major, the author believes that his exact words were “I think your strengths are in Sociology.”

The author would also like to acknowledge his wife, Kim, for her love and support. Kim almost did not follow the author to Gainesville, but the author cannot imagine life without her and their new baby girl, Alana Marie (“Peaches”), who has been a divine gift.

The author is deeply indebted to Dr. William Weltner, Jr., who unquestioningly accepted the author into his group with only two years remaining in his Ph.D. work. The author thanks him for giving him the opportunity, and it cannot go without saying that Dr. Weltner’s striving for the truth has made an indelible impression.

The author would also like to extend his thanks to Dr. Sam Colgate for allowing the him to work in his laboratory and for passing on to him his vast knowledge and skills. Thank you.

The author cannot say enough about the wonderful support staff at the University of Florida, especially the machine shop personnel. The projects the author has worked on would not have come to fruition without the skill and knowledge of Joe Shalosky, Todd Prox, and Mike Herlevich. We are truly spoiled to have access to these people.

Thanks also goes out to the author's cohorts and friends at UF. Dr. Aaron Williams, Dr. Heather Weimer, Dr. John Graham, Johnny Evans, and especially Dr. Richard Van Zee who might be the single most impressive scientist I have been associated with.

The author cannot forget about the "crue" from Illinois State University ("the Illinois mafia") who will always be apart of the author's life; David E. Kage, Dr. Nick Kob, Dr. Richard Burton, Dr. Eugene Wagner, Dr. Scott Kassel, and Ben Novak.

The author must also acknowledge the National Science Foundation (NSF) for financial support.

TABLE OF CONTENTS

	Page
ACKNOWLEDGEMENTS	ii
ABSTRACT	vi
CHAPTERS	
1 ELECTRON SPIN RESONANCE (ESR) THEORY	1
Classical Description	1
Quantum-Mechanical Treatment	2
2 THE NATURE OF A SPIN PROBE UNDER THE INFLUENCE OF SUPERCRITICAL CARBON DIOXIDE (CO ₂)	11
General Description of Supercritical Fluids.....	11
Introduction.....	12
Experimental	14
Results and Discussion	18
Conclusion	23
3 VIBRATIONAL SPECTROSCOPY THEORY	50
Classical Description	50
Quantum-Mechanical Treatment	53
4 INFRARED SPECTRA OF Nb ¹² C, Nb ¹³ C AND NbO ₂ MOLECULES MATRIX ISOLATED IN RARE GAS MATRICES.....	58
Introduction	58
Experimental	59
Results and Discussion	60

The Ground State ($^2\Delta_{3/2}$) Vibrational Properties of Nb ¹² C and Nb ¹³ C	67
The NbO ₂ molecule	68
Conclusion	72
5 DENSIMETER	74
Introduction.....	74
Thermodynamic Relationships	75
First Principles	78
Design of Densimeter	80
Densimeter Development.....	84
Experimental	89
Results.....	115
Conclusion	116
REFERENCES	122
BIOGRAPHICAL SKETCH	125

Abstract of Dissertation Presented to the Graduate School of the University of Florida in Partial Fulfillment of the Requirements for the Degree of Doctor of Philosophy

STABLE AND UNSTABLE MOLECULES UNDER SUPERCRITICAL AND CRYOGENIC CONDITIONS

By

Troy D. Halvorsen

August 1998

Chairman: Professor William Weltner, Jr.

Major Department: Chemistry

The electron spin resonance spectra of a spin label (di-tertiary butyl nitroxide, DTBN) dissolved in supercritical carbon dioxide were obtained. By investigating the band shapes of the spectra, information about the nature of the solvent can be inferred. Comparison to simulated spectra provided a means of interpreting these data.

The spectra of Nb¹²C, Nb¹³C and NbO₂ in argon, krypton and neon matrices were obtained using Fourier Transform infrared spectroscopy (FTIR). The resulting spectra were assigned through comparison of the isotopic shifts in vibrational frequencies.

A prototype high pressure densimeter was designed, built and successfully tested with argon and carbon dioxide around ambient temperatures and pressures up to 1800 psia.

CHAPTER 1

ELECTRON SPIN RESONANCE (ESR) THEORY

Classical Description

Classically speaking, an atom may possess electronic orbital motion which creates a magnetic dipole (μ). The description of a dipole moment induced by general angular momentum is given in equation 1, where p_L is the orbital angular momentum, c is the velocity of light, and e and m are the elementary charge and fundamental mass of an electron, respectively. The dipole moment is therefore proportional to the magnitude and

$$\mu_L = \left(\frac{-e}{2mc} \right) p_L \quad (1)$$

direction of the orbital angular momentum (p_L) and is scaled by a term more commonly referred to as the gyromagnetic ratio ($\gamma = -e/2mc$).

The intrinsic magnetic moment associated with an electron regardless of motion has been termed “spin.” The dipole moment associated with the spin of an electron is represented in equation 2, and it should be noted that the gyromagnetic ratio has an additional scaling factor of 2, which is added to account for its anomalous behavior. The contributions of spin (S) and orbital angular momenta (L) can couple to give a resultant total angular momentum (J) that can interact with an applied or local magnetic field. The energy of a magnetic dipole that is “perturbed” by a magnetic field is given classically by equation 3.

$$\mu_s = 2\left(\frac{-e}{2mc}\right)p_s \quad (2)$$

$$E = -\mu \cdot H \cos \theta \quad (3)$$

Quantum mechanics has relegated the angle θ (with respect to the dipole moment and magnetic field) to discrete space-fixed orientations. There are $2J + 1$ orientations of the total angular momentum (J) with projections of $m_J\hbar$ along the magnetic field axis, where m_J can assume values of $m_J = J, J - 1, \dots, -J$. The angular momentum coincident with the field are therefore the integral multiples of $p_z = m_J\hbar$. The dipole moment coincident with the magnetic field can then be rewritten as in equation 4. Here the term $(eh/4\pi mc = \beta_e)$ has been defined as the Bohr magneton. Therefore, the Zeeman energies

$$\mu_H = -2\left(\frac{e\hbar}{4\pi mc}\right)m_S \quad (4)$$

for a magnetic dipole in a magnetic field are given in equation 5, where a quantum electrodynamics correction needs to be included in lieu of the constant factor of 2. This correction is deemed the g-factor ($g_e = 2.0023$).

$$E = -\mu_H \cdot H = 2\beta_e m_S H = g_e \beta_e m_S H \quad (5)$$

Quantum-Mechanical Treatment

The simplest, yet the most rigorous and instructive manner in which to introduce the theory of Electron Spin Resonance (ESR) is to investigate the spin system of the simplest chemical entity known; the interaction of an electron (fermion) with a proton (fermion), routinely known as the ground state hydrogen atom (1H). In this case, the spin of the electron ($S = \frac{1}{2}$) does not solely produce fine structure, but may also interact with

the spin of the nucleus ($I = \frac{1}{2}$ in this case) to give hyperfine structure and therefore affords a rich example of this intricate interaction that is common to ESR. Furthermore, the Hamiltonian for the spin degrees of freedom of a hydrogen atom is not complicated by the anisotropies of the g-tensor and hyperfine interaction tensor (A) due to the lack of spin-orbit coupling and the spherical nature of the electronic ground state. Thus, the terms needed in the Hamiltonian are represented in equation 6.

$$\hat{H} = g_e \beta_e H^T \cdot \hat{S} + A_o \hat{S}^T \cdot \hat{I} - g_n \beta_n H^T \cdot \hat{I} \quad (6)$$

$g_e \beta_e H^T \cdot \hat{S}$ = electron Zeeman term

$A_o \hat{S}^T \cdot \hat{I}$ = hyperfine interaction term

$g_n \beta_n H^T \cdot \hat{I}$ = nuclear Zeeman term

When the z-axis is chosen to be the axis of space-quantization and coincident with the magnetic field (H), the Hamiltonian transforms via equation 7. With the use of the general raising and lowering operators (equations 8 and 9), equation 7 converts into

$$\hat{H} = g_e \beta_e H \cdot \hat{S}_z + A_o (\hat{S}_z \cdot \hat{I}_z + \hat{S}_y \cdot \hat{I}_y + \hat{S}_x \cdot \hat{I}_x) - g_n \beta_n H \cdot \hat{I}_z \quad (7)$$

final functional form, which is represented in equation 10. The Hamiltonian that has been

$$\hat{J}_+ \equiv \hat{J}_x + i\hat{J}_y \quad (8)$$

$$\hat{J}_- \equiv \hat{J}_x - i\hat{J}_y \quad (9)$$

constructed will operate on the four independent basis functions $| M_S, M_I \rangle$ for the

$$\begin{aligned} \hat{H} = & g_e \beta_e H \cdot \hat{S}_z + A_o \left[\hat{S}_z \cdot \hat{I}_z + \frac{1}{2} (\hat{S}_+ \cdot \hat{I}_- + \hat{S}_- \cdot \hat{I}_+) \right] \\ & - g_n \beta_n H \cdot \hat{I}_z \end{aligned} \quad (10)$$

hydrogen atom in the manner indicated in equation 11. The evaluation of the matrix

$$\langle M_S, M_I | \hat{H} | M_S', M_I' \rangle \quad (11)$$

elements have been worked out previously,¹ and the nonzero elements are contained below in equations 12-16. The resultant 4 x 4 matrix, depicted in Figure 1.1, can be

$$\langle M_S | \hat{S}_z | M_S \rangle = M_S \quad (12)$$

$$\langle M_I | \hat{I}_z | M_I \rangle = M_I \quad (13)$$

$$\langle M_S \pm 1, M_I | \hat{S}_{\pm} \hat{I}_{\pm} | M_S, M_I \rangle = M_I [S(S+1) - M_S(M_S \pm 1)]^{1/2} \quad (14)$$

$$\begin{aligned} & \langle M_S \pm 1, M_I \pm 1 | \hat{S}_{\pm} \hat{I}_{\pm} | M_S, M_I \rangle = \\ & [S(S+1) - M_S(M_S \pm 1)]^{1/2} \cdot [I(I+1) - M_I(M_I \pm 1)]^{1/2} \end{aligned} \quad (15)$$

$$\begin{aligned} & \langle M_S \pm 1, M_I \mp 1 | \hat{S}_{\pm} \hat{I}_{\mp} | M_S, M_I \rangle = \\ & [S(S+1) - M_S(M_S \pm 1)]^{1/2} \cdot [I(I+1) - M_I(M_S \mp 1)]^{1/2} \end{aligned} \quad (16)$$

solved as a secular determinant. To give a lucid representation of its solution, the matrix has been block factored along the diagonal. The two (1 x 1) diagonal elements give the following energies (equations 17 and 18), and the remaining (2 x 2) determinant can be

$$E_{\alpha(e)\alpha(n)} = + \frac{1}{2} g_e \beta_e H + \frac{1}{4} A_o - \frac{1}{2} g_n \beta_n H \quad (17)$$

$$E_{\beta(e)\beta(n)} = - \frac{1}{2} g_e \beta_e H + \frac{1}{4} A_o + \frac{1}{2} g_n \beta_n H \quad (18)$$

expanded and solved to produce the energies shown in equations 19 and 20. Note that the brackets that surround these particular eigenvalues (equations 19 and 20) indicate that they are only true eigenvalues in the limit of high magnetic field. In reality, the two states are linear combinations of the eigenstates $[\alpha_{(e)}\beta_{(n)}]$ and $\beta_{(e)}\alpha_{(n)}$ and their "purity" is

$$\begin{bmatrix}
 & [\alpha(e), \alpha(n)] & [\alpha(e), \beta(n)] & [\beta(e), \alpha(n)] \\
 [\alpha(e), \alpha(n)] & \begin{pmatrix} 1/2 g\beta H + 1/4 A_o \\ -1/2 g_n \beta_n H \end{pmatrix} & \begin{pmatrix} 0 \\ 0 \end{pmatrix} & \begin{pmatrix} 0 \\ 0 \end{pmatrix} \\
 & \hline
 & \begin{pmatrix} 1/2 g\beta H - 1/4 A_o \\ + 1/2 g_n \beta_n H \end{pmatrix} & \begin{pmatrix} 1/2 A_o \\ 0 \end{pmatrix} & \begin{pmatrix} 0 \\ 0 \end{pmatrix} \\
 & \hline
 & \begin{pmatrix} 1/2 A_o \\ -1/2 g\beta H - 1/4 A_o \\ -1/2 g_n \beta_n H \end{pmatrix} & \begin{pmatrix} 0 \\ 0 \end{pmatrix} & \begin{pmatrix} -1/2 g\beta H + 1/4 A_o \\ + 1/2 g_n \beta_n H \end{pmatrix}
 \end{bmatrix}$$

Figure 1.1. The spin Hamiltonian matrix for the Hydrogen atom.

$$E_{\{\alpha_{(e)}\beta_{(n)}\}} = -\frac{1}{4} A_o + \frac{1}{2} \left[(g_e \beta_e + g_n \beta_n)^2 H^2 + A_o^2 \right]^{1/2} \quad (19)$$

$$E_{\{\beta_{(e)}\alpha_{(n)}\}} = -\frac{1}{4} A_o - \frac{1}{2} \left[(g_e \beta_e + g_n \beta_n)^2 H^2 + A_o^2 \right]^{1/2} \quad (20)$$

contingent on the strength of the applied magnetic field. For instance, in a weak field the states are heavily mixed and strong coupling occurs between the states, which gives rise to four possible transitions.

The above solutions are referred to as the Breit-Rabi energies and are illustrated in Figure 1.2 as a function of low, intermediate, and high magnetic fields. The upper panel shows the low field region and the lower panel is at intermediate and high field. The Breit-Rabi equation was originally utilized to explain the transitional behavior of hydrogen atoms in a low-field molecular beam.²

The presence of off-diagonal terms in the matrix shown in Figure 1.1, necessarily indicates that the original basis functions are not all eigenfunctions of the Hamiltonian. A new basis set can obtained that are eigenfunctions of the Hamiltonian, which is based on a coupled representation of the individual angular momenta (see equation 21). This

$$\hat{F} = \hat{S} + \hat{I} \quad (21)$$

results in a total angular-momentum with a new set of quantum numbers, which can be represented in ket notation as $| F, M_F \rangle$. By inspection of the original matrix (see Figure 1.1), there are two functions that already exist as eigenfunctions by virtue of being diagonal elements ($|\alpha_{(e)}, \alpha_{(n)}\rangle$ and $|\beta_{(e)}, \beta_{(n)}\rangle$), and they can be represented in the coupled format as $| F, M_F \rangle = | 1,+1 \rangle$ and $| 1,-1 \rangle$. The remaining coupled

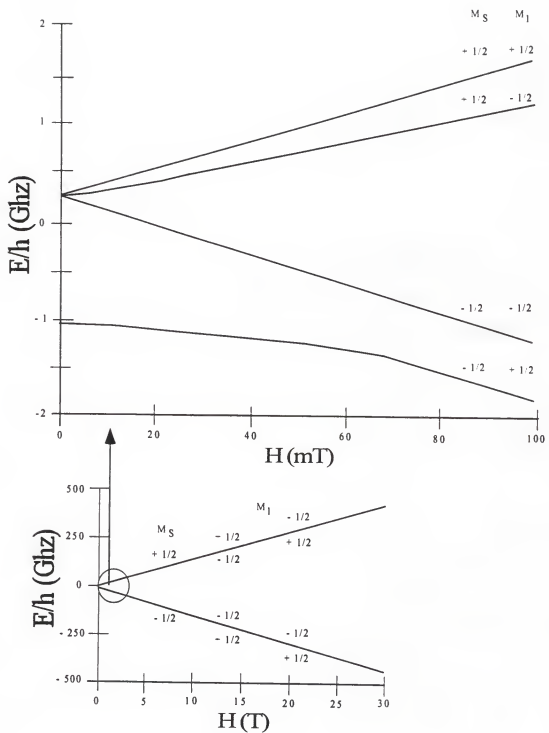


Figure 1.2. The Breit-Rabi diagram for the Hydrogen atom.

eigenfunctions $|F, M_F\rangle = |1,0\rangle$ and $|0,0\rangle$ can be solved for by the expansion of the (2×2) matrix as mentioned previously and represented as linear combinations below (equations 22 and 23).

The angle ω in the equations below determines the weight of hyperfine and Zeeman energies and can be extracted from the following relationships (equations 24 and

$$|1,0\rangle = \cos \omega |\alpha_{(e)}, \beta_{(n)}\rangle + \sin \omega |\beta_{(e)}, \alpha_{(n)}\rangle \quad (22)$$

$$|0,0\rangle = -\sin \omega |\alpha_{(e)}, \beta_{(n)}\rangle + \cos \omega |\beta_{(e)}, \alpha_{(n)}\rangle \quad (23)$$

25). At zero field, ($H = 0, \omega \rightarrow \pi / 4$), the two states are equally mixed and the

$$\sin 2\omega = |(1 + \xi^2)^{-1/2}| \quad (24)$$

$$\cos 2\omega = \xi |(1 + \xi^2)^{-1/2}| \quad (25)$$

$$\text{where } \xi = (g_e \beta_e + g_n \beta_n)H / A,$$

resultant linear combinations are given in equations 26 and 27. At the other extreme, as H approaches infinity ($H \rightarrow \infty, \omega \rightarrow 0$) the two states collapse into separate and distinct states (see equations 28 and 29).

$$|1,0\rangle = \frac{1}{2} (|\alpha_{(e)}, \beta_{(n)}\rangle + |\beta_{(e)}, \alpha_{(n)}\rangle) \quad (26)$$

$$|0,0\rangle = \frac{1}{2} (|\alpha_{(e)}, \beta_{(n)}\rangle - |\beta_{(e)}, \alpha_{(n)}\rangle) \quad (27)$$

$$|1,0\rangle = |\alpha_{(e)}, \beta_{(n)}\rangle \quad (28)$$

$$|0,0\rangle = |\beta_{(e)}, \alpha_{(n)}\rangle \quad (29)$$

Transitions in an ESR experiment can be induced with a "perturbing" interaction of electromagnetic radiation. A resonance condition is achieved when the frequency of this incident radiation exactly matches the energy difference between an initial and final state (equation 30). The intensity of this transition is the square of the matrix elements of

$$\hbar\nu = E_{final} - E_{initial} \quad (30)$$

the perturbing radiation between the initial and final states (equation 31). The operator in

$$|\langle initial | \hat{H}_1 | final \rangle|^2 \quad (31)$$

equation 31, which represents the incident radiation, is defined formally (equation 32) as the total dipole moment operator ($-\hat{\mu}^T$) dotted into the linearly polarized oscillating magnetic field (H_1). The above equation then transforms into final form as shown in equation 33.

$$\hat{H}_1 = -\hat{\mu}^T \cdot H_1 \quad (32)$$

$$\hat{H}_1 = (g\beta_e \hat{S} - g_n \beta_n \hat{I})^T \cdot H_1 \quad (33)$$

Low field transitions are quite different in terms of their selectivity and intensities due to the coupling of states to give the effective quantum numbers: $| F, M_F \rangle$. In essence there are four transitions with the selection rules of $\Delta M_F = \pm 1$ by virtue of H_1 being \perp to H (when $H // z$ and $H_1 // x$) where the transition operator becomes equation 34. A typical evaluation of a low field transition matrix element and corresponding

$$\hat{H}_1 = g\beta_e H_1 \hat{S}_x - g_n \beta_n H_1 \hat{I}_x \quad (34)$$

intensity is given in equations 35, 36, and 37 for the transition $| 1, -1 \rangle \rightarrow | 1, 0 \rangle$. The

$$\langle \beta_{(e)}, \beta_{(n)} | \hat{S}_x | \alpha_{(e)}, \beta_{(n)} \rangle = \frac{1}{2} \quad (35)$$

$$\langle \beta_{(e)}, \beta_{(n)} | \hat{I}_x | \beta_{(e)}, \alpha_{(n)} \rangle = \frac{1}{2} \quad (36)$$

$$|1, -1\rangle \rightarrow |1, 0\rangle \text{ intensity } \propto (g\beta_e \cos \omega - g_n\beta_n \sin \omega)^2 \quad (37)$$

more common intermediate and high field transitions with $H_1 // x$ and $H_1 \perp H$ has a transition operator as denoted in equation 38 with a general matrix element given in equation 39. Thus, the selection rules for higher fields are in general $\Delta M_s = \pm 1$ and $\Delta M_I = 0$, and the intensity is the square of this element.

$$\hat{H}_1 = g\beta_e H_1 \hat{S}_x \quad (38)$$

$$\langle M_S, M_I | \hat{H}_1 | M_S', M_I' \rangle = g\beta_e H_1 \langle M_S | \hat{S}_x | M_S' \rangle \langle M_I | M_I' \rangle \quad (39)$$

A typical experimental arrangement due to technological constraints is to utilize a constant frequency source and to sweep a static field. A problem arises in this experiment in that the magnetic field is different for subsequent transitions. An excellent approximate solution³ to this situation is given in equation 40. With the values of g and v , this equation can be solved for A_s . It must be noted that if $A_s/g > 0$ then the $M_I = -1/2$ line occurs at fields higher than $M_I = +1/2$, and the reverse is true if $A_s/g < 0$.

$$H = \frac{A_o}{g\beta_e} \frac{1}{1 - \left(\frac{A_o}{2hv}\right)^2} \cdot \left[-M_I \pm \left\{ M_I^2 + \left[1 - \left(\frac{A_o}{2hv}\right)^2 \right] \left[\left(\frac{hv}{A_o}\right)^2 - \left(I + \frac{1}{2}\right)^2 \right] \right\}^{1/2} \right] \quad (40)$$

CHAPTER 2
THE NATURE OF A SPIN PROBE UNDER THE INFLUENCE OF SUPERCRITICAL
CARBON DIOXIDE (CO₂)

General Description of Supercritical Fluids

The behavior of pure liquids and gases are in general fairly well characterized, but the conceptual understanding of a supercritical fluid is somewhat esoteric. There has been some evidence in the literature⁴⁻¹⁴ that supercritical fluids undergo "clustering" or local density augmentation particularly near the critical point, which may explain some of the unusual macroscopic behavior of these elusive fluids. A substance in the supercritical state (especially approaching the critical point) seems to lose any homogenous identity by undergoing time and spatial-dependent fluctuations in density. Extreme morphological changes in the fluid with little or no change in the temperature or the pressure of the system. (i.e.; the singular nature of the isothermal compressibility at this locale on the phase diagram), would seem to indicate a struggle on the molecular level for the more appealing "microscopic" phase of the moment.

These extreme molecular environments under the auspices of a single phase affords these fluids unique properties that can be intermediate between a gas and a liquid. This is evident by the fact that these fluids can possess the solvating power of a condensed phase (solvation generally scales logarithmically with density), but on the other hand may exhibit the mass transport properties (diffusivity and viscosity) of a gas.

This unique combination of solvent properties has led many authors^{5,15,16} to describe the nature of a supercritical solvent as “tunable.” In this case, the “tunability” refers to the thermodynamic timescale. But, what is truly happening on a faster timescale? To fully realize the potential of supercritical fluids, a fundamental understanding at the molecular level must be realized over a wide range of temperatures, pressures, and densities in and near the supercritical region. Only after this has occurred will the potential of supercritical fluids be revealed. A microscopic feel of these systems seems to be a necessity. This is partly due to the extensive commercial interest in supercritical fluids as a superlative alternative to traditional halogenated solvents because of their recyclability and relatively benign activity towards the environment.

Introduction

The recent investigative fervor into the nature of supercritical fluids has created some controversy^{17,18} about the true behavior of these systems at or near supercritical conditions. It is somewhat accepted that pure supercritical fluids possess some degree of solvent-solvent clustering.⁴⁻¹⁴ But, what is more speculative is the existence of solute-solute association¹⁹ when a dilute solute is introduced into a supercritical system. The essence of the question is how does the supercritical solvent treat the impurity? Does the supercritical system ignore the presence of the impurity and continue to self-cluster or does the solvent fully solvate the solute as it clusters? Is there some degree of solute association even in an extremely dilute situation where tiny time and spatial-dependent reaction centers are created with the presence of a surrounding modulatory bath of supercritical solvent structure? One can envision four or more possible scenarios:

1) solvent clustering with disregard to the solute impurity (without solute association) 2) solvent density augmentation around individual solute molecules that tends to hinder or enhance the transport of the solute (which may or may not be dependent on the solvent's location on the phase diagram) 3) solute association with minor solvent clustering and 4) solute association with solvent density augmentation around a solute cluster. These are just some of the questions that we wish to address and to begin to answer in this monograph.

The idea of critical clustering has been bantered about between authors who have argued for and against its existence with seemingly varying degrees of conviction. Randolph et al.¹⁷ initially reported evidence of critical clustering in and near supercritical ethane based on enhanced spin exchange rate constants of a spin probe. On the other hand, Batchelor¹⁸ has investigated the spin-rotation line broadening mechanism of very dilute ($\sim 1 \times 10^{-5}$ M) solutions of supercritical hexane and ethanol via a spin probe. Batchelor¹⁸ has argued that the spin-rotation mechanism is a more reliable indicator of critical clustering rather than spin exchange on the basis that an enhanced spin exchange can also be promoted via the onset of gas phase kinetics (and not necessarily critical clustering).

More recently, Randolph et al.¹⁹ have pointed out that without the presence of solute-solute association, their results for rotational diffusion models do not produce reasonable results. They have argued that previous investigators⁵⁻¹⁴ have ascribed enhanced rotational diffusion times in various supercritical media to solvent-solute density augmentation almost exclusively, but they (Randolph et. al.) stress that the

experimental results they have obtained do not make physical sense unless solute association is occurring since the local density enhancement far exceeds liquid densities. In this regard, the above authors have conceded previously the likely possibility that solute-solute clustering is probably dependent on the Lennard-Jones interaction potentials of the particular combination of solvent and solute.¹⁷

Thus, in order to begin to address the apparently rich phenomena outlined above and to try to corroborate or dispute some of the claims of the previous investigators, we have undertaken an investigation to explore some of the dynamical properties of a spin probe (di-tertiary butyl nitroxide, DTBN) under the influence of supercritical carbon dioxide (CO₂). Carbon dioxide has been chosen because of its amenable supercritical conditions (T_c = 31.0 °C, P_c = 1070.1 psi and ρ_c = 0.467 g/mL)²⁰ and its popularity as an exemplary alternative solvent.

Experimental

A high-pressure ESR cell fabricated (see Figure 2.1) from 6 mm O.D. and 2 mm I.D. quartz capillary tubing traversed a transverse electric (TE102) ESR cavity and was mounted horizontally (The ESR cavity was mounted in this fashion to minimize the gravitational effect on the concentration near the critical point,²¹ and all of the remaining components of the system are coplanar to within approximately 1") between the poles of an electromagnet. The ESR cell was connected to ancillary components (see Figure 2.2) of the system via 1/16" stainless steel tubing. This entire system was enclosed by a carefully constructed insulated foamboard enclosure and was subsequently sealed with a commercial foam sealant to create a semi-permeable insulating structure that would fully

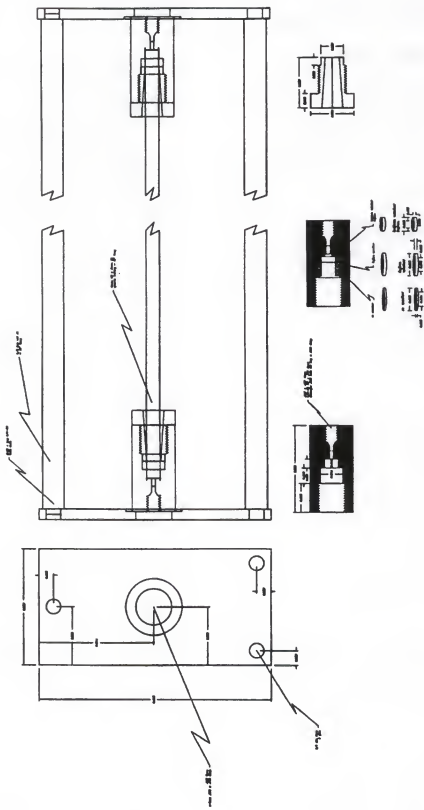


Figure 2.1. The high pressure ESR cell.

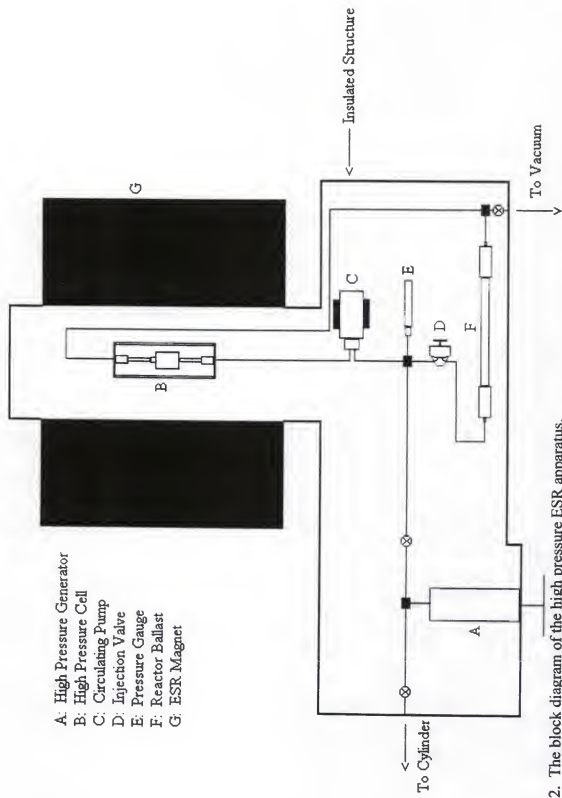


Figure 2.2. The block diagram of the high pressure ESR apparatus.

encompass all of the above mentioned components. The temperature of the subsequent air bath was regulated and controlled through the operation of two power resistors (nominally 110 W) that were suspended within the insulated volume and three 6" circulatory fans that were run at a high rate for thorough mixing. The temperature was monitored by two calibrated resistance temperature devices (Omega, model IPT100K2010) that were placed within the enclosed environment. The air bath was thermostatted to within ± 0.2 °C. The pressure of the apparatus could be varied by a piston (High Pressure Equipment, standard model 62-6-10) and monitored with a strain gauge pressure transducer (Omega, model PX612 5KGV) to within ± 2 psi.

To obtain supercritical conditions of carbon dioxide the apparatus was first evacuated and flushed several times to ensure that contamination did not occur. The vessel was then charged with fresh CO₂ (Scott Specialty Gases, Instrument Grade 99.99%) up to the maximum pressure of the CO₂ cylinder and was further pressurized with the use of liquid nitrogen to facilitate the condensation of CO₂. The temperature was then brought up to the desired supercritical isotherm and a specific pressure was obtained.

At this point, a high pressure circulating pump (Micropump, model 1805T-415A) was initiated to begin the circulation of the CO₂ through the high pressure system. An equilibration period of at least two hours ensured that the fluid had reached thermal equilibrium. After this allotted period, di-tertiary butyl nitroxide (DTBN, Aldrich, 90%tech. grade) was introduced into the volume via a high pressure injection valve (Valco, model C2-2306) equipped with a 20 μ L injection loop. The circulating pump

ensured mixing of the DTBN and carbon dioxide. The pressure and temperature were then noted as the starting conditions, and the concentration of CO₂ was calculated by the appropriate P,V_m,T measurements (based on a total volume of 140 ± 1 mL) by Wagner et.al.²⁰ The accurate determination of the CO₂ concentration was needed to calculate the mole fraction of DTBN relative to CO₂. The weight fractions of DTBN to CO₂ were well within the range of solubility.²²

After the equilibration period, ESR spectra were recorded with the following experimental arrangement: an X-band frequency generator (Varian E102 Microwave Bridge) was coupled to a horizontally mounted TE102 cavity and placed 90° relative to a permanent static field (Varian V-3601 Electromagnet). The field was modulated at 100 kHz with a modulation amplitude of 1 G. The center field was set at 3225 G and swept over a 50 G range. After a spectrum was recorded at a particular pressure along an isotherm, the mixture of carbon dioxide and DTBN was slowly leaked via a leak valve from the system to obtain a new pressure. In this way, a constant mole fraction of CO₂ and DTBN was maintained in order to monitor the behavior of supercritical CO₂ along an isotherm over a wide range of pressures (and thus densities) to see the response of the fluid with a constant number of probe molecules at each pressure. This procedure would give a similar thermal profile for each pressure and density.

Results and Discussion

The two dominant line broadening mechanisms that contribute to the overall linewidth in these systems will be spin-rotation at dilute concentrations and spin

exchange at higher concentrations. It has been pointed out¹⁸ that spin-rotation might be a better indicator of critical clustering rather than spin exchange because enhanced spin exchange near the critical density might just be an indication of the onset of gas phase behavior rather than a sign of clustering. A deconvolution of these two line-broadening mechanisms is difficult in concentrated samples because of the overwhelming contribution from spin-exchange, which tends to mask the residual linewidth (and thus the contribution) from the spin-rotation. Therefore, solute-solute and/or solute-solvent clustering might best be explored with the observation of spin exchange (v_{ex}) and correlation time (τ_c) simultaneously (with the treatment of spin-rotation as a residual Gaussian linewidth contribution). In this manner, clustering pertinent to the spin probe will be shown more conclusively than by study of either independently. Correlation times essentially reflect the extent of time-averaging of the anisotropies caused by the modulation activity of the environment surrounding the spin active species. Therefore, correlation time will manifest itself in a completely different manner (essentially an m_i dependence in the ESR spectra) in relation to spin exchange (usually an equal broadening of all lines considered).

To try and circumvent the above mentioned problem, a "modest" amount (~ 1E-5 mole fraction) of spin label (DTBN) was introduced into supercritical carbon dioxide (CO_2) to try and account for both the spin exchange (v_{ex}) and correlation time (τ_c). It has been reasoned that the dominant mechanism at higher pressures should be mostly spin exchange, but as the pressure is decreased towards the critical pressure, spin-rotation

might have a more significant contribution. Specifically, spin-rotation should be less obvious at higher pressures, and more pronounced at lower pressures as there will be a marked decrease in viscosity (η) as an isotherm is traversed (spin-rotation has a T/η dependence). Therefore, if normal behavior prevails spin-rotation will contribute to an overall larger linewidth as pressure decreases. Therefore, the spin exchange frequency that will be modeled might be slightly higher (due to the increased contribution of spin-rotation at lower pressures) than the absolute frequency, but nonetheless the rate constant of spin exchange (k_e) versus correlation time (τ_c) should still show the trend sought. Otherwise, increased spin exchange would not necessarily point to solute association, because it might simply be explained by the onset of gas phase behavior and an increase in transport phenomena. Therefore, the prudent representation of the data would be the 3-D plot of spin exchange (v_{ex}) and correlation time (τ_c) versus pressure (or density).

The general strategy was to prepare a supercritical bath at selected pressures (and thus densities) along an isotherm and to extract the motional behavior (i.e.; v_{ex} , τ_c , and residual linewidth ($lw_{res.}$)) of the spin probe from ESR spectra. This would be performed over several temperatures and mole fractions to determine their dependence or lack thereof on the dynamical properties.

The ESR spectra were simulated with the use of modified version of Freed's²³ simulation program that have been tailored specifically for nitroxide spin labels. Freed's program explicitly accounts for spin exchange and correlation time and all other relaxation processes can be taken into account by a residual linewidth. The simulation of

these spectra were performed by inputting the g and A tensors of DTBN extracted from the powder spectra of Griffiths and Libertini.²⁴ The spin exchange rate (v_{ex}), diffusional rate coefficients (d_{xy} , d_{zz}), and the residual linewidth (lw_{res}) were varied to optimize the fit of the experimental spectra. The spin exchange rate and diffusional rate coefficients were used to calculate the respective rate constants of spin exchange (k_c) and rotational correlation times (τ_c) appropriate for each fit (see equations 41-43).

$$v_{ex} = k_e [DTBN]^2 \quad (41)$$

$$(d_{xy} d_{zz})^{1/2} = d_{rot} \quad (42)$$

$$\tau_c = \frac{1}{6d_{rot}} \quad (43)$$

Figures 2.3-2.7 show the series of digitized ESR spectra with their respective simulations for a series of pressures along the 34 °C isotherm at $\chi = 6.1E-5$ (where χ is defined as mole fraction). Table 2.1 shows a summary of the pertinent thermodynamic and motional data for these spectra (Figures 2.3-2.7). Figures 2.8-2.11 show a series of spectra and simulations again at 34 °C isotherm, but at $\chi = 5.4E-5$. Table 2.2 shows a summary of these data. Figures 2.12-2.15 show spectra and simulations at 40 °C ($\chi = 5.4E-5$) and Table 2.3 shows a summary of these spectra. Finally, Figures 2.16-2.18 show 50 °C spectra ($\chi = 6.4E-5$) and Table 2.4 shows a compilation of these data.

Figures 2.19-2.24 illustrate the nature of the correlation time and spin exchange behavior with respect to density, temperature, and concentration. At all three temperatures there is a general increase in correlation time (τ_c) as the reduced density is traversed from high density to low density, except for the 34 °C isotherm at $\chi = 5.4\text{E-}5$ (compared to $\chi = 6.1\text{E-}5$). Here there is a general increase in the correlation time until the reduced density approaches approximately 0.68.

The rate constants (k_r) also increase in general as reduced density is traversed (except for the above mentioned example) for the 34 °C and 40 °C isotherms. The 50 °C isotherm shows a general increase then a small decrease in rate constants that mirror a subtle increase in correlation time.

Figure 2.24 shows the temperature dependence of the correlation times at a constant mole fraction of 5.4 E-5. This comparison suggests that the interaction of the solvent becomes more frequent at the lower temperature (34 °C) at an inflection point of reduced density at approximately 0.68 and nearly equals the correlation time found at the higher temperature (40 °C) at this density. Overall, the correlation time is higher for the lower temperature up until this point.

The temperature dependence of the rate constants (Figure 2.23) at the same mole fraction of 5.4 E-5 indicates that the spin exchange rate is lower in general for the lower temperature until this reduced density is reached (0.68). At this point, a precipitous increase in the rate constant is seen for the 34 °C isotherm that slightly exceeds the rate constant observed at the 40 °C isotherm.

Conclusion

It appears that the rate constants (k_e) for spin exchange generally increase as the reduced density decreases at the lower temperatures (34 °C and 40 °C) nearer the critical temperature ($T_c = 32.1$ °C). A precipitous increase in k_e is witnessed at the 34 °C isotherm and mole fraction of $\chi = 6.1$ E-5 at a reduced density of approximately 0.68. A concomitant increase in correlation time (τ_c) is generally prevalent at these temperatures also. This behavior indicates a clustering phenomenon (either solvent-solute or solute-solute), otherwise the correlation time should decrease as the rate constant increases if gas phase behavior is truly the cause of an increased rate constant. The exception to this behavior is the lower mole fraction ($\chi = 5.4$ E-5) at 34 °C. At a reduced density 0.68, there is a distinct decline in τ_c with an increase in k_e . This would indicate an onset of gas phase behavior instead of clustering and points to solute-solute clustering as a possible cause of enhanced rate constants in the higher mole fraction ($\chi = 6.1$ E-5) experiment at 34 °C.

The behavior at 50 °C indicates that there is a marked increase in rate constants and correlation times at a higher reduced density ($\rho_R \sim 1.0$) and then a leveling off at lower reduced density. This would indicate that clustering behavior might occur at higher reduced densities when the temperature is further removed from the critical temperature.

The related errors in the spin exchange rate constants (k_e) and correlation times (τ_c) that are inherent in the simulations can be accounted for with a generous range of ± 0.5 Lmol⁻¹s⁻¹ × 10⁻¹³ for k_e and ± 5 ps for τ_c respectively.

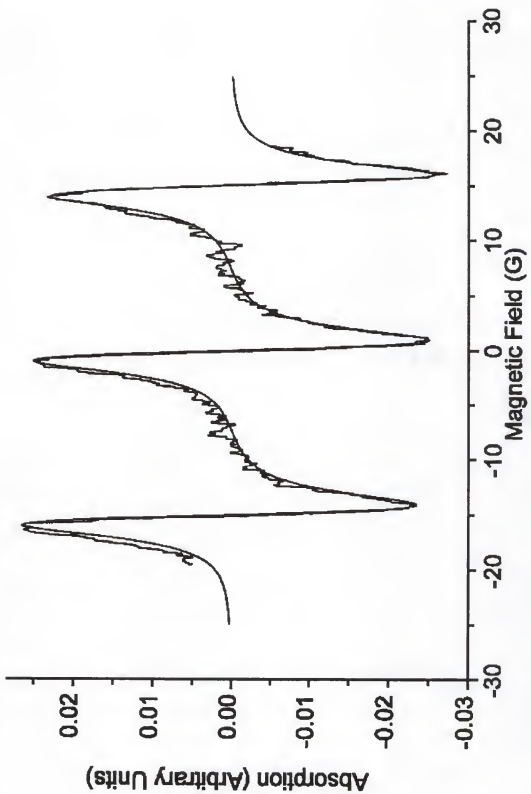


Figure 2.3. The ESR spectrum of DTBN in supercritical CO_2 at $T = 34^\circ\text{C}$ and $P = 1275 \text{ psi}$.

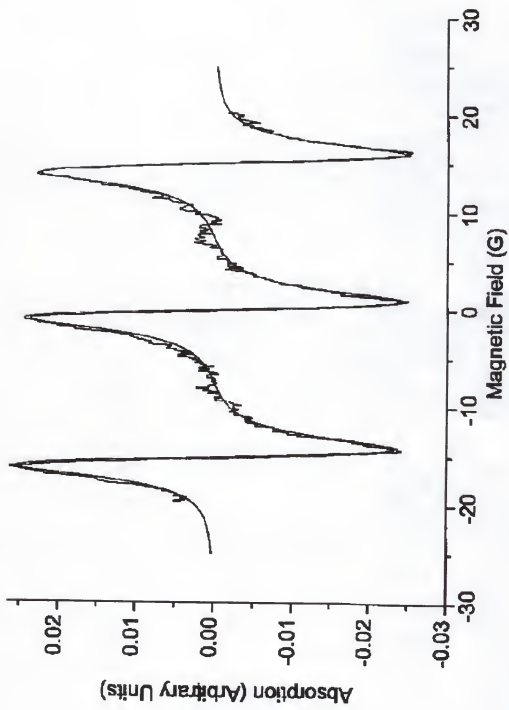


Figure 2.4. The ESR spectrum of DTBN in supercritical CO_2 at $T = 34^\circ\text{C}$ and $P = 1167 \text{ psi}$.

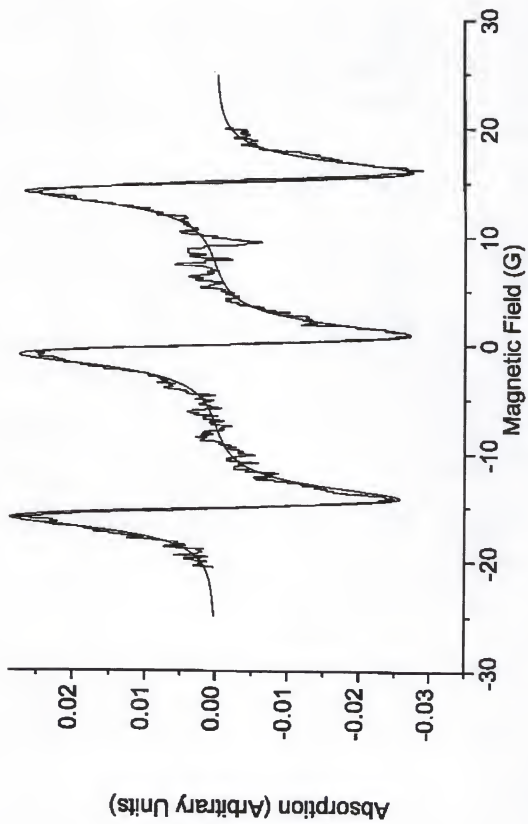


Figure 2.5. The ESR spectrum of DTBN in supercritical CO_2 at $T = 34^\circ\text{C}$ and $P = 1090 \text{ psi}$.

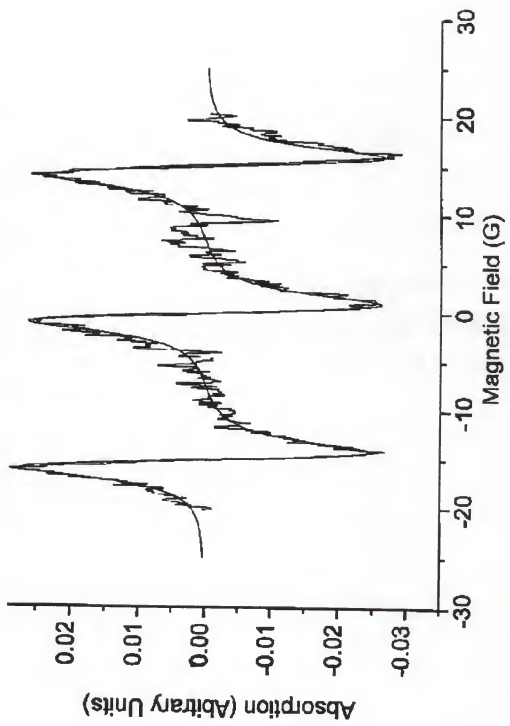


Figure 2.6. The ESR spectrum of DTBN in supercritical CO_2 at $T = 34^\circ\text{C}$ and $P = 1070 \text{ psi}$.

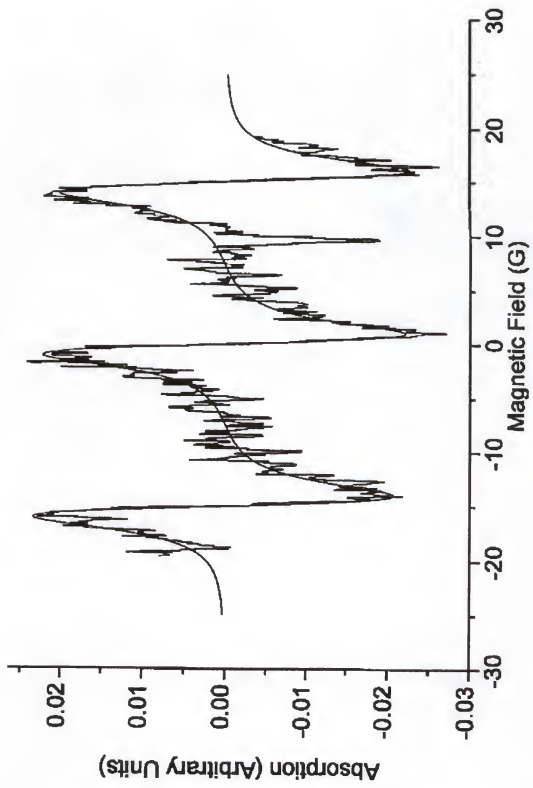


Figure 2.7. The ESR spectrum of DTBN in supercritical CO_2 at $T = 34^\circ\text{C}$ and $P = 1050 \text{ psi}$.

Table 2.1. Summary of thermodynamic and dynamic properties of CO_2/DTBN along the $T = 34^\circ\text{C}$ isotherm with a $\chi = 6.1 \times 10^{-5}$ mole fraction.

Pressure (psi)	ρ (g/mL)	ρ_{R}	$[I]_{\text{DTBN}}(M)$	$v_e(\text{s}^1)$	$k_e(\text{Lmol}^{-1}\text{s}^1) \times 10^{13}$	$\tau_e(\text{ps})$	$Iw_{\text{res}}(\text{G})$
1275	0.672	1.43	9.21 E-4	2.0 E7	2.3	18	0.7
1167	0.576	1.23	7.97 E-4	2.0 E7	3.1	23	0.9
1090	0.294	0.629	4.09 E-4	2.3 E7	13.7	23	0.7
1070	0.271	0.580	3.76 E-4	2.4 E7	16.9	23	0.7
1052	0.252	0.539	3.50 E-4	2.5 E7	20.4	27	0.8

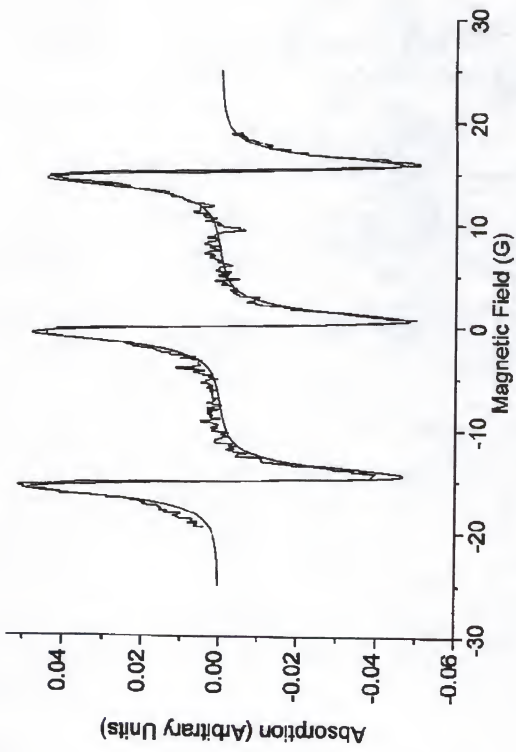


Figure 2.8. The ESR spectrum of DTBN in supercritical CO_2 at $T = 34^\circ\text{C}$ and $P = 1545 \text{ psi}$.

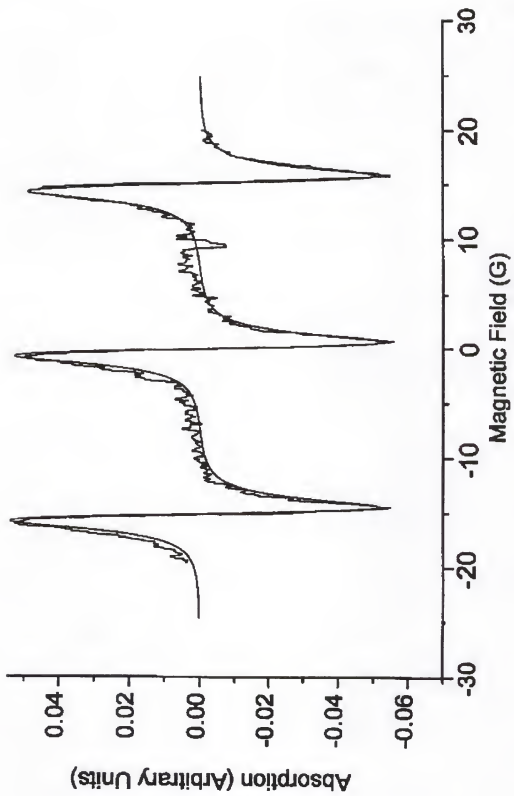


Figure 2.9. The ESR spectrum of DTBN in supercritical CO₂ at T = 34 °C and P = 1350 psi.

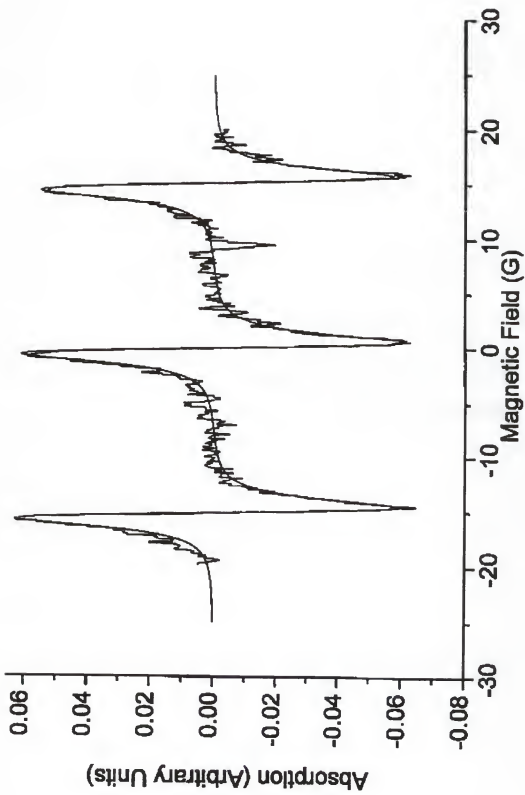


Figure 2.10. The ESR spectrum of DTB in supercritical CO_2 at $T = 34^\circ\text{C}$ and $P = 1100 \text{ psi}$.

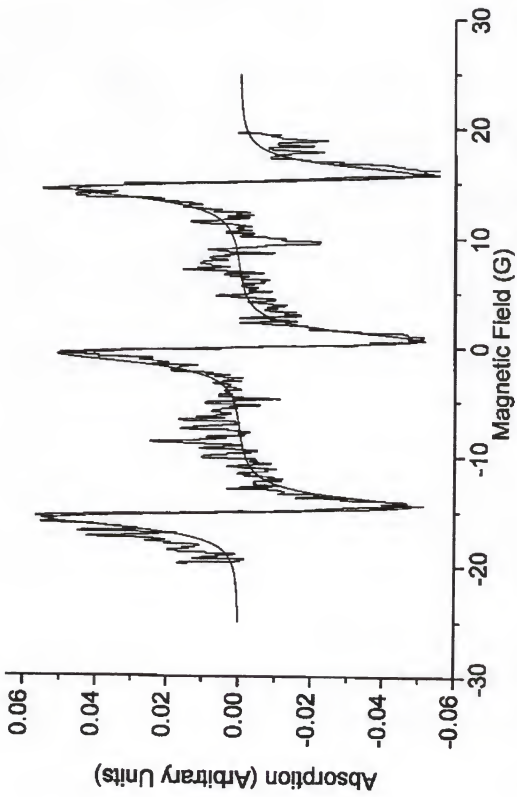


Figure 2.11. The ESR spectrum of DTBN in supercritical CO_2 at $T = 34^\circ\text{C}$ and $P = 1080 \text{ psi}$.

Table 2.2 Summary of thermodynamic and dynamic properties of CO₂/DTBN along the T = 34 °C isotherm with a $\chi = 5.4E-5$ mole fraction.

Pressure (psi)	ρ (g/mL)	ρ_R	[] _{DTBN} (M)	v_{ex} (s ⁻¹)	k_e (Lmol ⁻¹ s ⁻¹) $\times 10^{-13}$	τ_e (ps)	Iw_{res} (G)
1545	0.746	1.59	9.21 E-4	1.0 E7	1.1	23	0.8
1350	0.700	1.49	8.59 E-4	1.1 E7	1.4	27	0.7
1100	0.311	0.665	3.82 E-4	1.0 E7	6.8	37	0.65
1080	0.282	0.603	3.45 E-4	2.1 E7	17.6	25	0.35

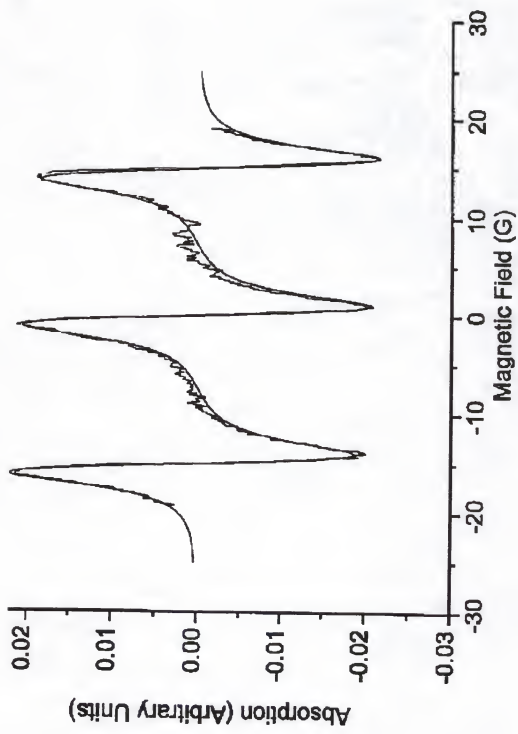


Figure 2.12. The ESR spectrum of DTBN in supercritical CO₂ at T = 40 °C and P = 1895 psi.

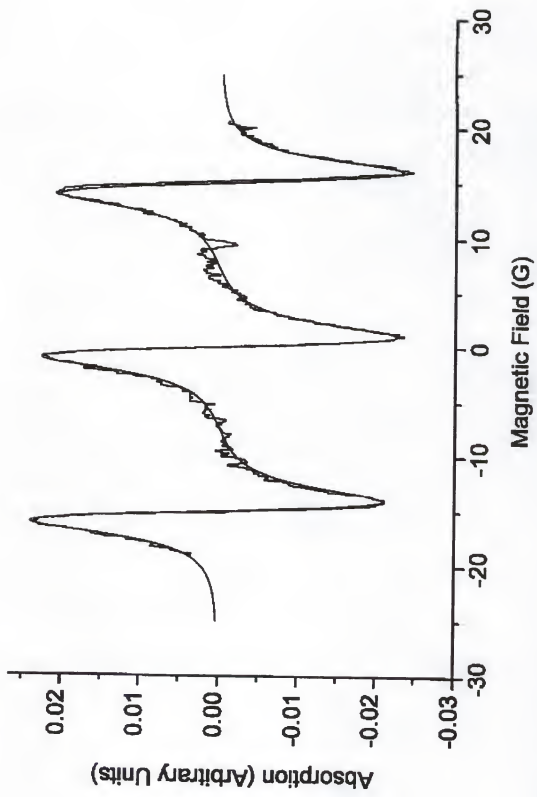


Figure 2.13. The ESR spectrum of DTBN in supercritical CO₂ at T = 40 °C and P = 1547 psi.

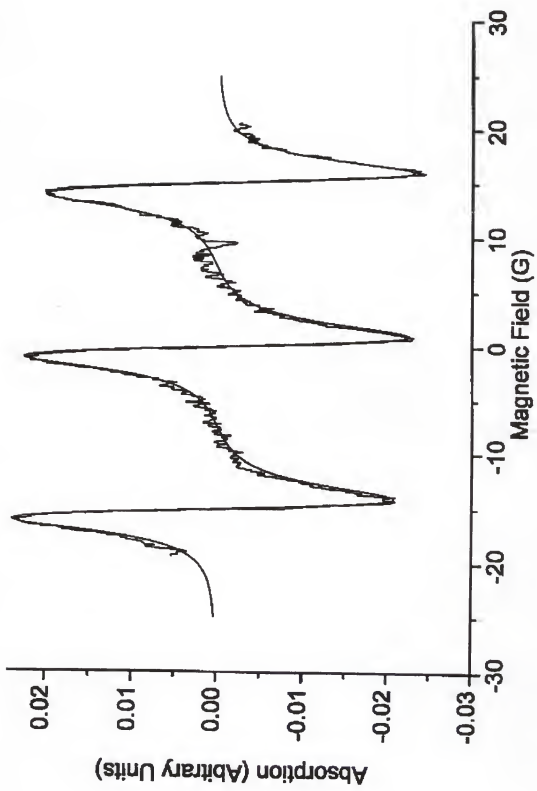


Figure 2.14. The ESR spectrum of DTBN in supercritical CO_2 at $T = 40^\circ\text{C}$ and $P = 1355 \text{ psi}$.

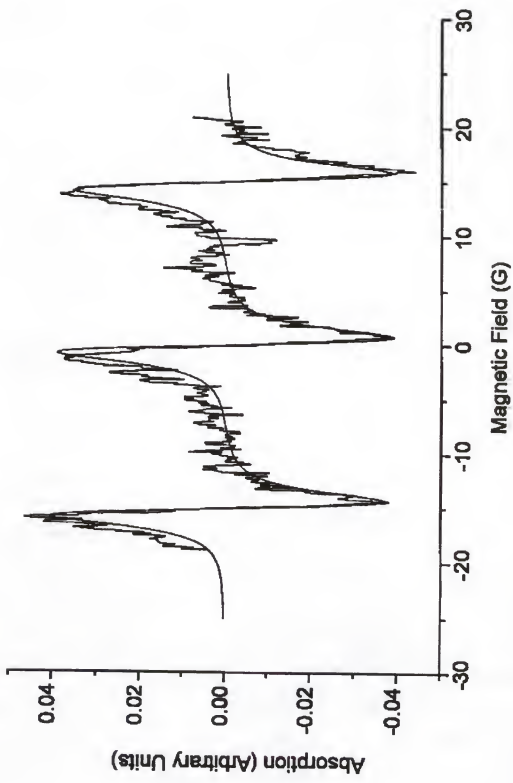


Figure 2.15. The ESR spectrum of DTBN in supercritical CO_2 at $T = 40^\circ\text{C}$ and $P = 1160 \text{ psi}$.

Table 2.3 Summary of thermodynamic and dynamic properties of CO₂/DTBN along the T = 40 °C isotherm with a $\chi = 5.4E-5$ mole fraction.

Pressure (psi)	ρ (g/mL)	P_k	[] _{DTBN} (M)	v_{ex} (s ⁻¹)	k_e (L mol ⁻¹ s ⁻¹) $\times 10^{13}$	τ_c (ps)	Iw_{res} (G)
1895	0.745	1.59	9.21 E-4	3.5 E7	4.1	16	0.5
1547	0.669	1.43	8.22 E-4	3.0 E7	3.4	18	0.5
1355	0.561	1.20	6.89 E-4	3.0 E7	6.3	23	0.6
1160	0.282	0.603	3.47 E-4	2.0 E7	16.6	27	0.55

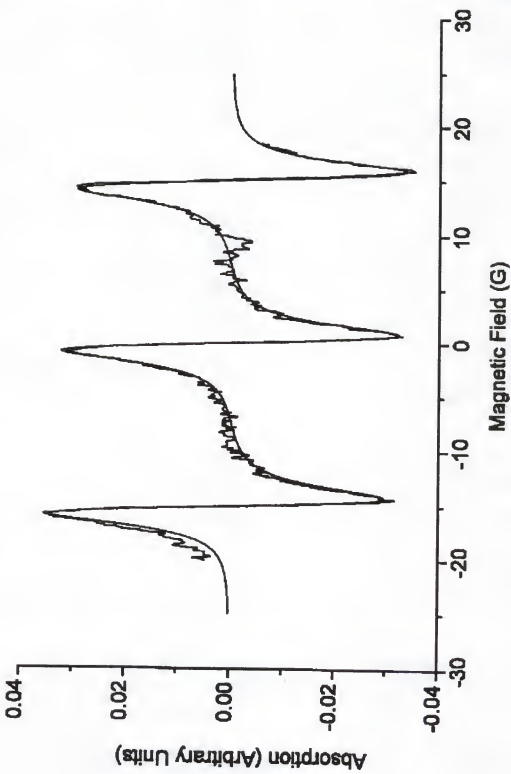


Figure 2.16. The ESR spectrum of DTBN in supercritical CO_2 at $T = 50^\circ\text{C}$ and $P = 1875 \text{ psi}$.

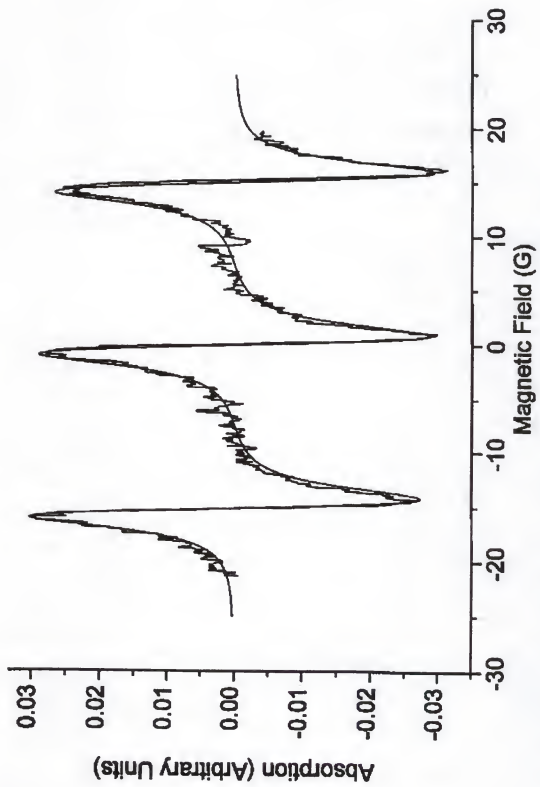


Figure 2.17. The ESR spectrum of DTBN in supercritical CO_2 at $T = 50^\circ\text{C}$ and $P = 1555 \text{ psi}$.

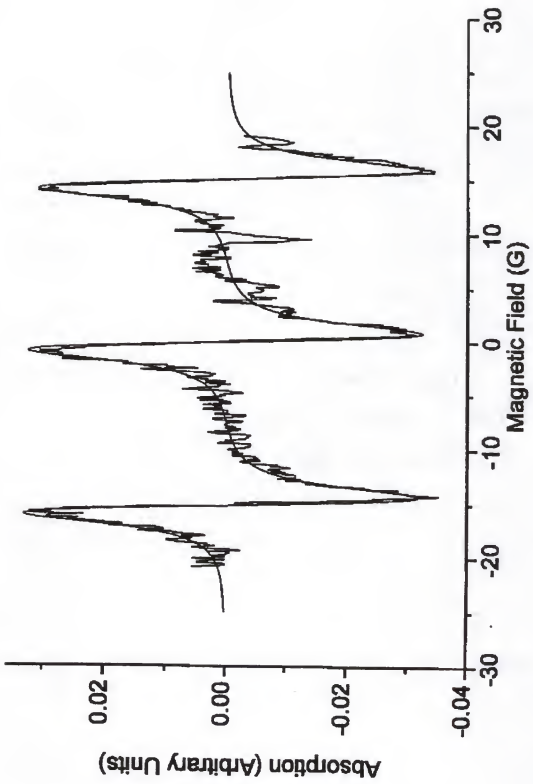


Figure 2.18. The ESR spectrum of DTBN in supercritical CO_2 at $T = 50^\circ\text{C}$ and $P = 1343 \text{ psi}$.

Table 2.4 Summary of thermodynamic and dynamic properties of CO_2/DTBN along the $T = 50^\circ\text{C}$ isotherm with a $\chi = 6.4\text{E-}5$ mole fraction.

Pressure (psi)	ρ (g/mL)	P_R	$[I]_{\text{DTBN}}$ (M)	$v_{\text{ex}}(\text{s}')$	$k_e(\text{Lmol}^{-1}\text{s}')$ $\times 10^{13}$	$\tau_c(\text{ps})$	Iw_{res} (G)
1875	0.633	1.35	9.21 E-4	3.2 E7	3.7	8	0.5
1555	0.471	1.01	6.85 E-4	2.2 E7	4.6	16	0.6
1343	0.307	0.657	4.46 E-4	9.0 E6	4.5	18	0.6

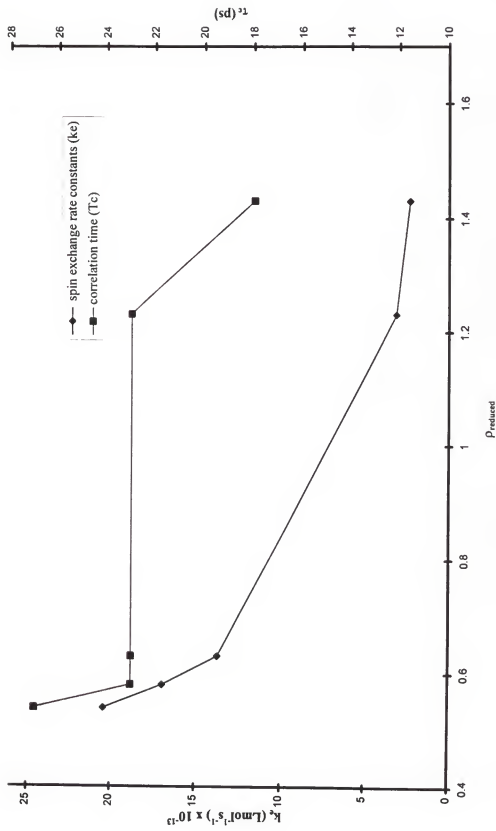


Figure 2.19. The dynamic properties at $T = 34^\circ\text{C}$ and $\chi = 6.1 \times 10^{-5}$.

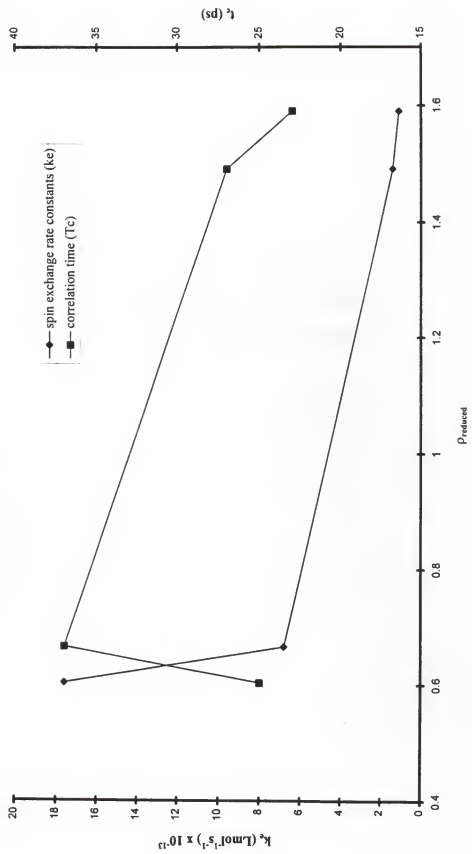


Figure 2.20. The dynamic properties at $T = 34^\circ\text{C}$ and $\chi = 5.4 \times 10^{-5}$.

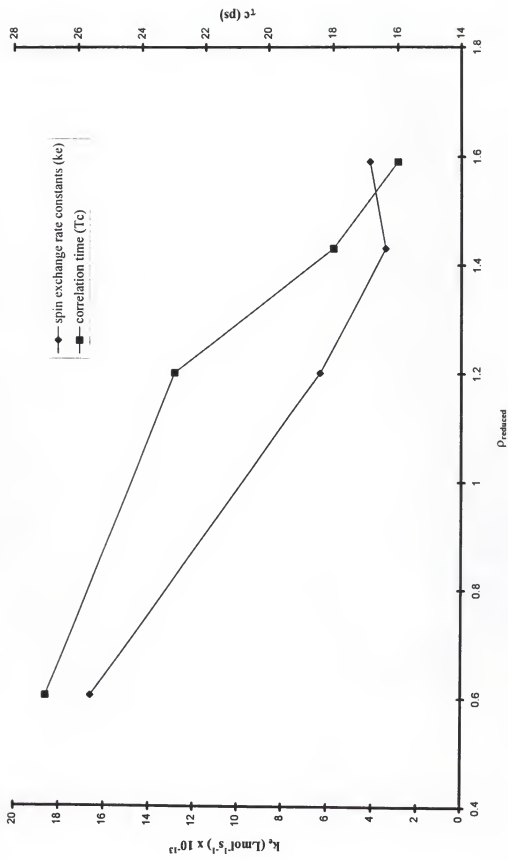


Figure 2.21. The dynamic properties at $T = 40^\circ\text{C}$ and $\chi = 5.4 \times 10^{-5}$.

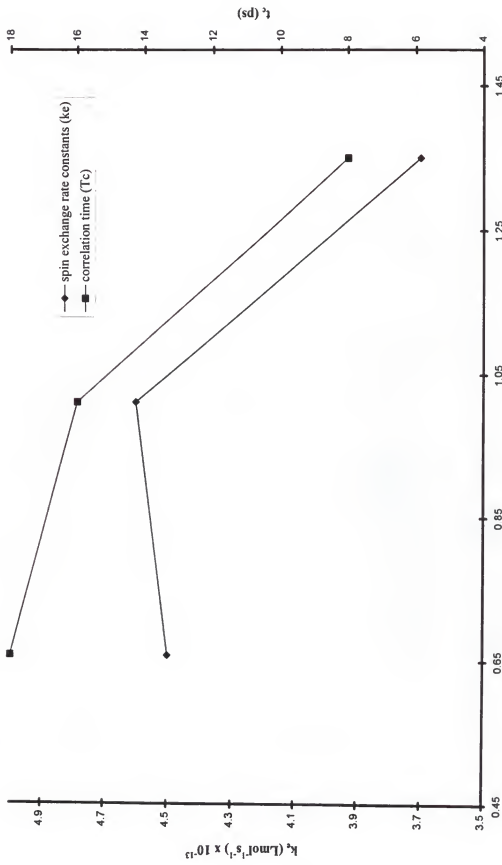


Figure 2.22. The dynamic properties at $T = 50^\circ\text{C}$ and $\chi = 6.4 \text{ E-}5$.

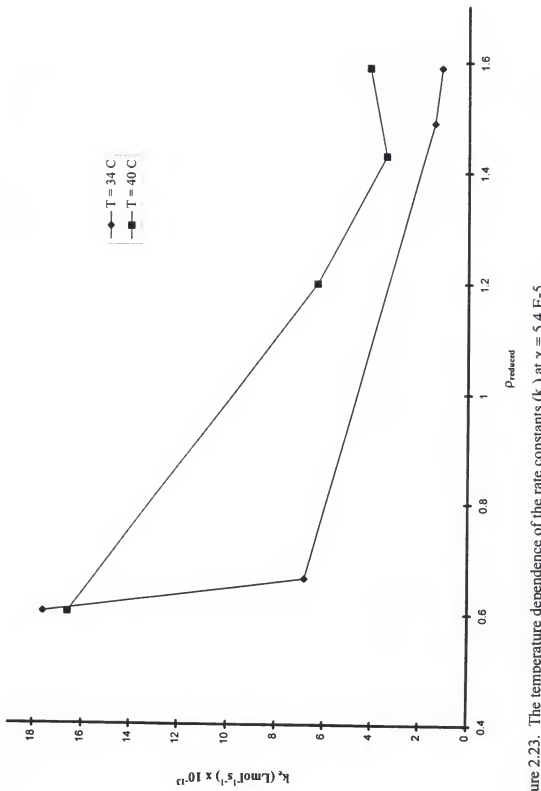


Figure 2.23. The temperature dependence of the rate constants (k_e) at $\chi = 5.4 \times 10^{-5}$.

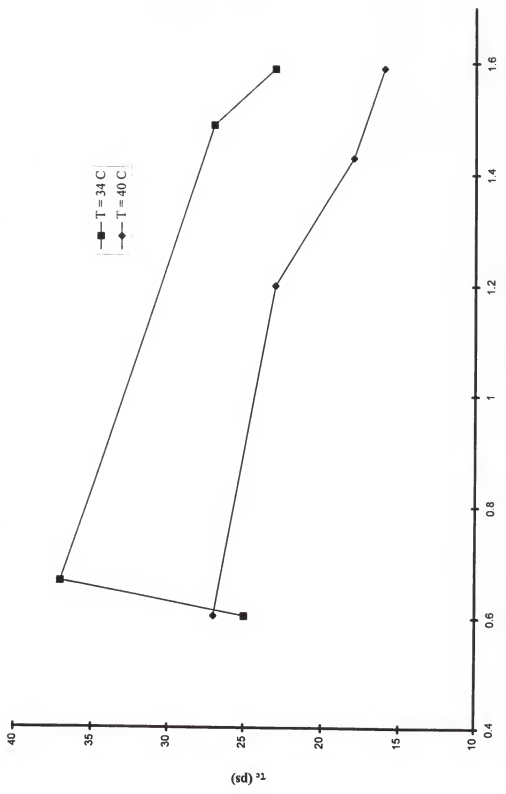


Figure 2.24. The temperature dependence of the correlation time (τ_c) at $\chi = 5.4 \text{ E-}5$.

CHAPTER 3

VIBRATIONAL SPECTROSCOPY THEORY

Classical Description

The origin of vibrational activity stems from the seemingly simple interaction of two mass points that are physically connected through space and are originally at an equilibrium position (see Figure 3.1). The impending motion (in the absence of torque or any rotational motion) can be described by classical harmonic motion, which is defined as the movement that results when a force acting on a body is proportional to the displacement of the body from an equilibrium position.²⁵ Implementing Newton's First Law to describe this motion (see equation 44) results in a homogenous 2nd order differential equation. The general solution to type of differential problem is given in

$$\bar{F} = m\ddot{x} = m \frac{\partial^2 x}{\partial t^2} - kx \quad (44)$$

equation 45. If this eigenfunction is differentiated twice, the result is given in equation

$$x = A \cos(\omega t + \delta) \quad (45)$$

46. The angular frequency associated with the linear motion of this system can be related

$$m(-\omega^2 [A \cos(\omega t + \delta)]) \quad (46)$$

simply to the ratio of the force constant (i.e.; the scalar response to the force acting on the body) to the mass (shown in equation 47). The one-dimensional energy of a two-body

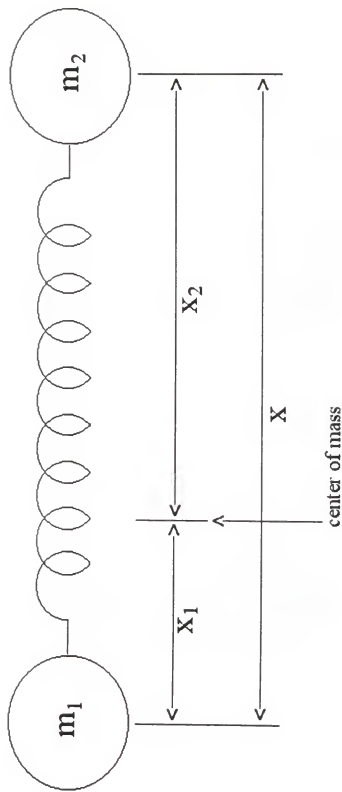


Figure 3.1. The two-body oscillator.

$$v = \frac{1}{2\pi} \left(\frac{k}{m} \right) \quad (47)$$

oscillator can be represented as shown in equation 48.

$$T = \frac{1}{2} m_1 \vec{v}_1^2 + \frac{1}{2} m_2 \vec{v}_2^2 + \frac{1}{2} kx^2 \quad (48)$$

\vec{v}_1 = linear velocity of m_1

\vec{v}_2 = linear velocity of m_2

$$\frac{1}{2} kx^2 = \text{classical potential integrated from } F = -\frac{\partial V}{\partial x}$$

By using the center-of-mass relationship (i.e.; $m_1x_1 = -m_2x_2$), differentiating with respect to time, and utilizing momenta in lieu of mass and velocity (equations 49 and 50),

$$m_1 \frac{dx_1}{dt} = -m_2 \frac{dx_2}{dt} \quad (49)$$

$$m_1 \vec{v}_1 = -m_2 \vec{v}_2 = p_1 = p_2 \quad (50)$$

the energy can be represented in terms of momenta (equation 51). The energy can be

$$T = \frac{p_1^2}{2m_1} + \frac{p_2^2}{2m_2} + \frac{1}{2} kx^2 \quad (51)$$

eventually reduced to a representation (equations 52 - 54) involving momentum (p) and

$$T = \frac{1}{2} \left[\frac{m_2 p^2 + m_1 p^2}{m_1 m_2} \right] + \frac{1}{2} kx^2 \quad (52)$$

$$\mu = \frac{m_1 m_2}{m_1 + m_2} \quad (53)$$

reduced mass (μ), which is commonly known as the classical Hamiltonian.

$$T = \frac{P^2}{2\mu} + \frac{1}{2} kx \quad (54)$$

Quantum-Mechanical Treatment

The classical Hamiltonian for a two-body interaction can be transformed into the quantum-mechanical operator via equation 55. The Hamiltonian in essence contains all

$$-\frac{\hbar^2}{2\mu} \nabla^2 \psi + V(x)\psi = E\psi \quad (55)$$

of the energetic information of the system, but the center-of-mass contribution to the kinetic energy operator in this instance has been excluded in this equation because it represents only a shift in the total energy of the system. When the cartesian coordinate system (x, y, z) is reconfigured into spherical polar coordinates (r, θ, ϕ), the Hamiltonian converts to equation 56, where \hat{J}^2 is the square of the angular momentum. The solution of this equation involves the selection of an appropriate wavefunction that is separated

$$-\frac{\hbar^2}{2\mu} \left[\frac{1}{r^2} \frac{\partial}{\partial r} r^2 \frac{\partial \psi}{\partial r} \right] + \frac{1}{2\mu r^2} \hat{J}^2 \psi + V(r)\psi = E\psi \quad (56)$$

into a radial and angular dependence (see equation 57, where Y_{JM} is the spherical harmonic).

$$\psi = R(r)Y_{JM}(\theta, \phi) \quad (57)$$

The one-dimensional radial Schrodinger equation is the result of this substitution (equation 58). An effective potential can be written to encompass the potential due to the

internuclear separation ($V(r)$) and a "centrifugal" potential²⁶ of the spherical harmonic

$$\frac{-\hbar^2}{2\mu} \frac{d}{dr} r^2 \frac{dR}{dr} + \left(\frac{\hbar^2 J(J+1)}{2\mu r^2} + V(r) \right) R = ER \quad (58)$$

$$V_{\text{eff}} = V(r) + V_{\text{cent}} \quad (59)$$

(equation 59). To simplify equation 58, the substitution of $S(r) = R(r)r$ gives equation 60.

$$\frac{-\hbar^2}{2\mu r^2} \frac{d^2 S}{dr^2} + \left(\frac{\hbar^2 J(J+1)}{2\mu r^2} + V(r) \right) S = ES \quad (60)$$

A rigorous solution to this equation for the corresponding energy levels and wavefunctions requires only a functional form of the potential ($V(r)$). Generally speaking the potential $V(r)$ encompasses the electronic energy $E_{\text{el}}(r)$ (obtained from the solution of the electronic Schrodinger equation) and the nuclear repulsion term (V_{NN}) (see equation 61). The parametric dependence of the electronic dependence E_{el} on r (and thus the lack

$$V(r) = E_{\text{el}}(r) + V_{\text{NN}} \quad (61)$$

of an analytical form for E_{el} and V_{NN}) has led to the empirical development of $V(r)$. A popular potential (Dunham potential²⁶) is a Taylor series expansion about r_e (equation 62). Typically $V(r_e)$ is set equal to zero (chosen arbitrarily) and therefore the first

$$V(r) = V(r_e) + \left. \frac{dV}{dr} \right|_{r_e} (r - r_e) + \frac{1}{2} \left. \frac{d^2 V}{dr^2} \right|_{r_e} (r - r_e)^2 + \dots \quad (62)$$

derivative is zero (equation 63). If the first term is the only one retained (equation 64) in the expression and J is set equal to zero, the harmonic oscillator solutions are obtained (equation 65), where $H_v(\alpha^{1/2}x)$ are the Hermite polynomials. The related eigenvalues are

$$\left. \frac{dV}{dr} \right|_{r_e} = 0 \quad (63)$$

given in equation 66 for the non-rotating harmonic oscillator.

$$V(r) = \frac{1}{2} k(r - r_e)^2 \quad (64)$$

$$k = \left. \frac{d^2 V}{dr^2} \right|_{r_e}$$

$$S = NvHv(\alpha)^{1/2} xe^{-\alpha x^2} \quad (65)$$

$$x = r - r_e$$

$$\alpha = \frac{\mu\omega}{\hbar}$$

$$N_v = \left[\frac{1}{2^v v!} \left(\frac{\alpha}{\pi} \right)^{1/2} \right]^{1/2}$$

$$E(v) = hv(v + 1/2) \quad (66)$$

$$v = \frac{1}{2\pi} \left(\frac{k}{\mu} \right)^{1/2}$$

Still another possible potential is the Morse potential (equation 67), which approaches a dissociation limit [V(r) = D] as r goes to infinity. Furthermore, the Morse potential can be solved analytically to give the following eigenvalues with harmonic and

$$V(r) = D(1 - e^{-\beta(r-r_e)})^2 \quad (67)$$

anharmonic terms for the harmonic oscillator (equation 68).

$$G(v) = \omega_e(v + \frac{1}{2}) - \omega_e \chi_e(v + \frac{1}{2})^2 \quad (68)$$

The prediction of allowed vibrational transitions involves the assessment of the dipole moment integral (equation 69) in which single primes denote upper levels and double primes denote lower states. If the dipole moment ($\mu(r)$) is represented as a Taylor series expansion (equation 70), the evaluation of this integral is given in equation 71. It is immediately evident that the first term on the right is equal to zero or 1, because the

$$Mv' v'' = \int \varphi'_{vib} \mu(r) \varphi''_{vib} dr \quad (69)$$

$$\mu = \mu_e + \left. \frac{d\mu}{dr} \right|_{r_e} (r - r_e) + \frac{1}{2} \left. \frac{d^2\mu}{dr^2} \right|_{r_e} (r - r_e)^2 + \dots \quad (70)$$

$$Mv' v'' = \mu_e \int \varphi'_{vib}^* \varphi''_{vib} dr + \left. \frac{d\mu}{dr} \right|_{r_e} \int \varphi'_{vib}^* (r - r_e) \varphi''_{vib} dr + \dots \quad (71)$$

vibrational wavefunctions are orthogonal. Of the remaining terms, the second term (which is the change in the dipole with respect to change in position evaluated at the equilibrium position (r_e)) contributes the most to the intensity of the transition (see equation 72).

$$I \propto |Mv' v''|^2 \propto \left| \left. \frac{d\mu}{dr} \right|_{r_e} \right|^2 \quad (72)$$

The remaining component that needs to be evaluated for a vibrational transition is the integral in equation 73. With the utilization of the harmonic oscillator wavefunctions and the recursion formula between Hermite polynomials (equation 74), the resultant integral is given in equation 75. The evaluation of this integral leads to the familiar

$$\int \varphi'_{vib}^* (r - r_e) \varphi''_{vib} dr \quad (73)$$

$$2xHn(x) = H_{n+1}(x) + 2nH_{n-1}(x) \quad (74)$$

vibrational selection rules of $\Delta v = \pm 1$ (fundamental bands only), because the Kronecker δ (in equation 75) is $v' = v + 1$ or $v - 1$.

$$\langle v' | x | v \rangle = \left(\frac{\hbar}{2m\omega} \right)^{1/2} \left[\sqrt{v + 1} \delta_{v', v+1} + \sqrt{v} \delta_{v', v-1} \right] \quad (75)$$

CHAPTER 4
INFRARED SPECTRA OF Nb¹²C, Nb¹³C, and NbO₂ MOLECULES ISOLATED IN
RARE GAS MATRICES

Introduction

The rudimentary architecture of "met-cars"²⁷ is the metal carbide diatom. Within this frame of reference, it is necessary to elucidate the basic interactions between the metal and carbon as a duet with and without the perturbing interactions of a solvent structure. With this in mind, the gas phase ground electronic state of Nb¹²C has recently been determined to be $^2\Delta_{3/2}$ by Simard et. al.,²⁸ confirming the original prediction of Weltner and Hamrick²⁹ based on electron spin resonance (ESR) studies of this radical in solid rare-gas matrices. In this specific case, it would have proven difficult to detect (via ESR) such a species in a rare-gas matrix without the "quenching" of the orbital angular momentum. A diatomic radical with an orbitally degenerate ground state (i.e., Π , Δ , etc.) is typically rendered undetectable in the ESR due to the subsequent diffuse nature of the signal. But, in some instances angular momentum can be "quenched" by an orthorhombic crystal field¹ which causes its properties in the matrix to approach that of a Σ molecule.

It is generally the case that rare-gas matrices at cryogenic temperatures provide the "mildest" of perturbations on the trapped guests,^{30,31} indicated by shifts from their gas phase vibrational frequencies and electronic levels being only a few percent.^{30,31}

However, if the molecule is highly ionic (as, for example, LiF) the molecule-matrix interaction can be large and the shifts in the solid state considerably larger. If this interaction is substantial and the molecule is sitting in an asymmetrical site in the matrix, then large anisotropic crystal field effects can also occur which effectively remove the axially-symmetric character of the electronic wavefunction, as referred to above. And, generally speaking the chemistry in the gas phase versus the condensed or solid phase can be radically different as is evident in gas versus condensed phase acidities of some mineral acids (e.g., HCl). The entrapment of these molecules in solid rare-gas matrices is integral to the complete understanding of the entire continuum of the chemistry between the isolated gas phase intrinsic properties and the intimate guest/host interactions of the solid and condensed phases.

The ground state of NbC has been calculated to have an exceptionally large dipole moment ($\mu = 6.06 \text{ D}$)²⁸ so that even without the quenching of the orbital angular momentum one can expect large matrix shifts for corresponding optical spectra when investigated in a matrix. Also, through spin-orbit effects there can be mixing of the lower states so that forbidden electronic transitions may be observable. With this in mind, we now wish to report the effects of the ground state vibrational frequencies ($\Delta G_{1/2}''$) of Nb^{12}C , Nb^{13}C , and NbO_2 when trapped in solid neon, argon, and krypton.

Experimental

The experimental setup has described in detail previously.³² In summary, mixtures of niobium and carbon (slightly rich in the metal) were pressed into pellet form

and vaporized with a highly focused Nd:YAG laser (Spectra Physics DCR-11) operating at 532 nm. The metal and carbon plume was co-condensed in rare gas matrices at a rate of approximately 10 mmol/hr over periods of 1 to 1.5 hour onto a gold-plated copper surface at 4 K. The IR spectra were measured via a vacuum FTIR spectrometer (Bruker IFS-113V) equipped with a liquid-nitrogen-cooled MCT detector ($400\text{-}4800\text{ cm}^{-1}$) used in conjunction with a KBr beam splitter. The spectra were taken with a resolution of 2 cm^{-1} (or in some cases 1 cm^{-1}) and a scan number typically of 200.

The niobium powder was purchased from Electronic Space Products International (99.9% purity). Carbon-12 was obtained as a spectroscopic grade electrode in graphite form and ground into a fine powder. Amorphous carbon-13 (99% purity) was purchased from Isotech and outgassed at $1400\text{ }^{\circ}\text{C}$ for 1 hour before use. The matrix gases were obtained from the following vendors; neon (Matheson, 99.9995% purity); argon (Airco 99.999% purity); and krypton (Praxair, 99.9985% purity).

Results and Discussion

Kr

The most conclusive evidence for the formation of Nb^{12}C and Nb^{13}C was in a krypton matrix shown in Figure 4.1 (and Table 4.1). Traces A and B show the absorption spectra in the stretching regions for the fundamental bands of Nb^{12}C (B) and Nb^{13}C (A) after annealing the spectra to 45 K and quenching to the original temperature of the deposition (4 K). By observing the similarities and differences between the two spectra, one can discern that the bands to the blue of the sharp band at 941.0 cm^{-1} in trace B are

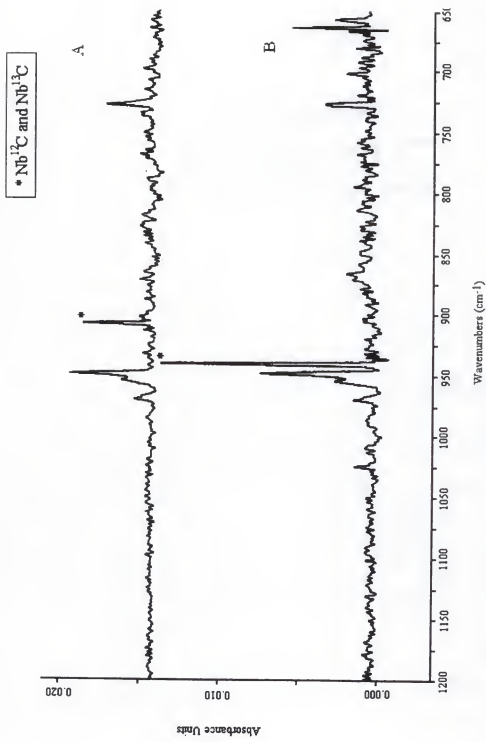


Figure 4.1. The IR spectra of Nb¹²C and Nb¹³C in krypton.

common to spectra A. Therefore, it is quite reasonable to remark that these absorptions are not due to any NbC containing products. The clear differences between the two spectra are: 1) the absorption at 941.0 cm^{-1} in the lower trace and 2) the absorption at 908.5 cm^{-1} in the upper panel, which corresponds very reasonably with the isotopic shifts that can be calculated by the usual harmonic relationship for diatomics represented in equation 76. Both of these absorptions are quite strong in their respective spectra and are

$$\nu_{13} = \nu_{12} \left(\frac{\mu_{12}}{\mu_{13}} \right) \quad (76)$$

absent in comparison with the isotopic counterpart. Therefore, these two absorptions have been confidently assigned to Nb^{12}C and Nb^{13}C respectively.

The strong peak at approximately 949 cm^{-1} has not been assigned, but it appears in traces A and B, therefore it is assumed that it is not a $\text{Nb}_{(n)}\text{C}_{(n)}$ species. It has also been assumed that the absorptions (the weak doublet at 970.3 and 967.6 cm^{-1}) that are at higher wavenumbers relative to the NbC species are due to the stretching frequency (ies) of NbO and/or NbO_2 . These transient species are prevalent in this type of experiment as has been remarked by Simard et. al.²⁸ and the personal experience of the investigators. Unfortunately, the characterization of these species in a krypton matrix has not been made to date, so it cannot be concluded for certain that these are $\text{NbO}_{(n)}$ impurities. The belief that this absorption is indeed due to NbO is based on the fact that these peaks are at slightly lower frequencies than those assigned to NbO in neon and argon matrices,^{33,37} which will be discussed further below. The weak absorption at 1024.5 cm^{-1} is again not believed to be a $\text{Nb}_{(n)}\text{C}_{(n)}$ because it appears periodically in both Nb^{12}C and Nb^{13}C spectra.

Ar

Figure 4.2 displays the spectra from experiments carried out in a argon matrix. Traces A and B show the results of the Nb¹³C and Nb¹²C experiments respectively. The stretching frequency due to Nb¹²C is assigned to the band at 952.2 cm⁻¹. The absence of this peak in the Nb¹³C spectra (trace A) gives further proof of this assignment. Likewise, the absorption at 917.7 cm⁻¹ that is clearly evident in the Nb¹³C traces is amiss in the Nb¹²C spectra.

Again, there are residual peaks blue-shifted relative to the above assignments. It can be said with certainty in this case that some of these are due to the fundamental modes of NbO. Green, Korfmacher, and Gruen³³ have previously assigned these peaks (971 cm⁻¹, 968 cm⁻¹, and 964 cm⁻¹) to NbO in an argon matrix. The three peaks have been attributed to NbO in different sites in the argon lattice. Note there is an extra peak at 974.6 cm⁻¹ that appears in the matrix containing Nb¹²C.

In the Nb¹²C trace it is evident that there are some transitions besides those attributed to Nb¹²C and NbO that do not appear in the top trace. The doublet that appears at 946.2 and 941.4 cm⁻¹ could possibly be Nb_(n)C, but the corresponding ¹³C substituted frequencies should be present and are apparently absent. Still, another possibility is that the Nb¹²C peaks are from molecules in different sites in the matrix. The relatively strong peak to the red of the assigned Nb¹³C peak (917.7 cm⁻¹) at 911.5 cm⁻¹ (which may also be the peak in the Nb¹²C trace at 913.3 cm⁻¹) cannot be definitely assigned. The two sets of triplets (913.1, 907.2, 901.1 cm⁻¹ and 873.8, 867.8, 859.6 cm⁻¹) that appear in the Nb¹²C

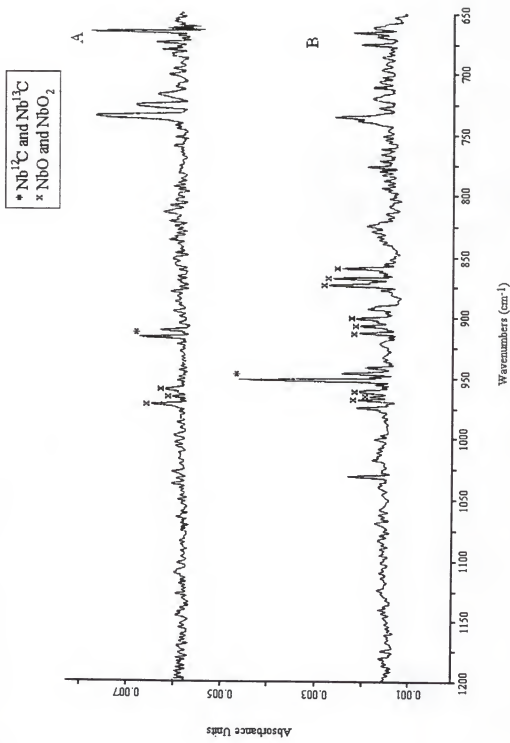


Figure 4.2. The IR spectra of Nb¹²C and Nb¹³C in argon.

spectrum, but do not appear in this specific Nb¹³C trace (but have been observed in other spectra of Nb¹³C) have been assigned to NbO₂, since it has been reported that in certain Knudsen cell/mass spectrometric experiments³⁴ that equal amounts of NbO and NbO₂ are observed to form on vaporization of Nb₂O₅. Further evidence for this conjecture is that the triplet pattern (presumably three sites) for both of these transitions mirror the behavior of NbO. If this is true, it is the first reported evidence of NbO₂ in a matrix experiment. This will be discussed further. Finally, the peak at 1030 cm⁻¹ is a transient peak that appears in both experiments although it does not appear in trace B for this particular experiment.

It is interesting to note that the gas phase vibrational frequency for NbO ($\Delta G_{1/2}''$) has been determined to be 981.3, cm⁻¹ by Gatterer, Junkes, Salpeter, and Rosen.^{35,36} This value is extremely close to the gas phase ground state vibrational frequency of Nb¹²C ($\Delta G_{1/2}'' = 980 \pm 15$ cm⁻¹) given by Simard et. al.²⁸ With all else considered, the position of the vibrational frequency in various matrices should be a measure of the relative strengths of interaction between NbC (and NbO) and the matrix.

Ne

The results in neon (Figure 4.3) are the least revealing. In trace B, the weak absorption at 983.0 cm⁻¹ is tentatively assigned to Nb¹²C. In the upper panel, low frequency shoulder of the doublet at 952.8 cm⁻¹ and 949.7 cm⁻¹ is assigned to the Nb¹³C stretch, based strictly on the calculated isotopic shift from the band at 983.0 cm⁻¹. Furthermore, the gas phase value given by Simard et. al.²⁸ is very close to the assignment

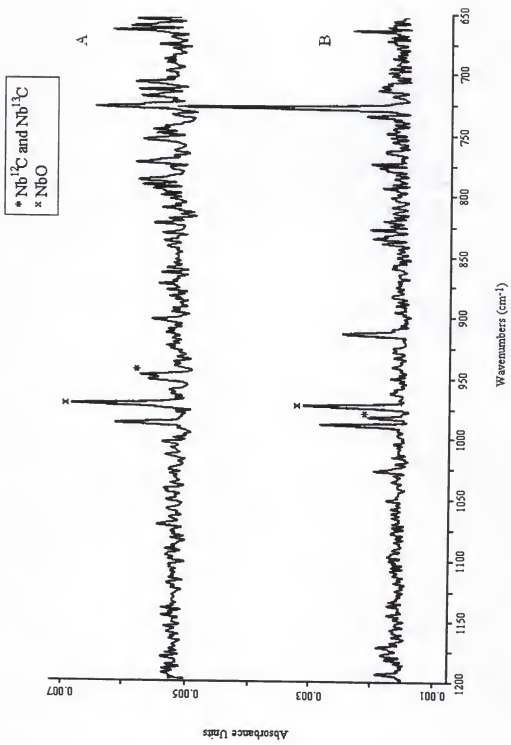


Figure 4.3. The IR spectra of Nb¹²C and Nb¹³C in neon.

in the neon matrix. This makes intuitive sense since neon is the least perturbing of the rare-gas matrices by virtue of the comparison of matrix shifted values for diatomic ground state vibrational frequencies and electronic transitions.^{30,31} Again, there are impurity peaks due to NbO, which in this case have been previously characterized by Brom, Durham, and Weltner.³⁷ They have assigned three absorptions due to sites in the matrix for NbO at 965.5, 973.0, and 977.1 cm⁻¹. In our spectra, it seems that the only site we see is the one at 973.6 cm⁻¹. This would not seem to be out of the realm of possibility since the matrices were prepared in dissimilar manners.³⁷ The peak at 989.4 cm⁻¹ that appears in both spectra has not been assigned and probably is not due to NbO since these peaks have been characterized previously, but it seems to be an impurity that cannot be related to any Nb_(n)C_(n) product either. The transition at 914.5 cm⁻¹ could possibly be due to NbO₂ since only one site is seen here for NbO (in contrast to the argon data).

The Ground State ($^2\Delta_{1/2}$) Vibrational Properties of Nb¹²C and Nb¹³C

Table 4.2 gives a summary of the ground state harmonic frequencies (ω_e) and their corresponding anharmonic corrections ($\omega_e \chi_e$) that were calculated from the experimentally observed $\Delta G''_{1/2}$ frequencies for the two isotopomers. The relationships used in these calculations are given in equations 77 - 80.³⁸ A comparison of the matrix and gas phase values are given along with harmonic force constants.

$$\Delta G''_{1/2}(\text{Nb}^{12}\text{C}) = v_m^{12} = \omega_e^{12} - 2\omega_e^{12}\chi_e^{12} \quad (77)$$

$$\omega_e^{13} = \rho \omega_e^{12} \quad (78)$$

$$\omega_e^{13}\chi_e^{13} = \rho^2 \omega_e^{12}\chi_e^{12} \quad (79)$$

$$\rho = (\mu^{12} / \mu^{13})^{1/2} = 0.9652 \quad (80)$$

The NbO₂ molecule

The fortuitous observation of NbO₂ in an argon matrix has given us a chance to speculate on the ground state of the NbO₂ molecule. The ground electronic state of NbO₂ has not been reported to our knowledge, but we would like to report the ground state vibrational frequencies of ν_1 and ν_3 , and cautiously assign the ν_2 bending mode. The symmetric stretch (ν_1) has three sites at 913.1, 907.2, and 901.1 cm⁻¹ (see Figure 4.2). The asymmetric stretch (ν_3) has three sites as well at 873.4, 867.8, and 859.6 cm⁻¹. The bending mode would be expected to have a weak transition to the red of the above absorptions. We have tentatively assigned the triplet around 518 cm⁻¹ (524.5, 517.7, and 510.6) to ν_2 (see Figure 4.4).

With the apparent observation of a symmetric and asymmetric stretch, a bent ground state seems to be in order. The bond angle of this ground state can be estimated via the ratio of the relative intensities of ν_3 and ν_1 with the assumptions made by Ozin et al.³⁹ Figure 4.5 shows the enhanced region of the NbO₂ stretching region of Figure 4.2.

$$\frac{I\nu_3}{I\nu_1} = \tan^2 \theta \left(\frac{M_{Nb} + 2M_O \sin^2 \theta}{M_{Nb} + 2M_O \cos^2 \theta} \right) \quad (81)$$

The ratio of ν_3 and ν_1 is based on the integrated intensities of the respective matrix sites. The intensity ratio was determined to be 1.71, which gives a bond angle of $2\theta = 103^\circ$. This value agrees quite reasonably with Spiridonov et. al. ($\theta = 101.6(3.3)$).⁴⁰

Surprisingly, a theoretical treatment of NbO₂ has not been cited in the literature to the best of our knowledge. The most recent experimental work on NbO₂ was an

Table 4.1. Observed IR bands (cm^{-1}) of niobium monocarbide and niobium dioxide in rare gas matrices.

Molecule	Neon	Argon	Krypton	Assignment
Nb ¹² C	983. ₀	952. ₂	941. ₀	$\Delta G''_{1/2}$
Nb ¹³ C	949. ₇	917. ₇	908. ₅	$\Delta G''_{1/2}$
NbO ₂		873. ₈ , 867. ₈ , 859. ₆		v_1 (sym. str.)
NbO ₂		913. ₁ , 907. ₂ , 901. ₁ ,		v_3 (asym. str.)
NbO ₂		524. ₅ , 517. ₇ , 510. ₆		v_2 (bending)

Table 4.2. Vibrational frequencies (cm^{-1}) of the ground state (${}^2\Delta_{3/2}$) of Nb¹²C and Nb¹³C in rare-gas matrices at 4 K.

Species	Parameter	Ne	Ar	Kr	Gas Phase ^a
Nb ¹² C	$\Delta G''_{1/2}$	983. ₀	952. ₂	941. ₀	980 \pm 15
	ω_e^{12}	1013. ₀	962. ₁	951. ₁	
	$\omega_e^{12} \chi_e^{12}$	15. ₀	4. ₉	5. ₀	
Nb ¹³ C	$\Delta G''_{1/2}$	949. ₇	917. ₇	908. ₅	
	ω_e^{13}	975.2	926.1	915.6	
	$\omega_e^{13} \chi_e^{13}$	12.8	3.4	3.5	
	$k^b (\text{mdyn/A})$	6.42	5.79	5.66	

^afrom reference 28.

^bcalculated from relationship in reference 38.

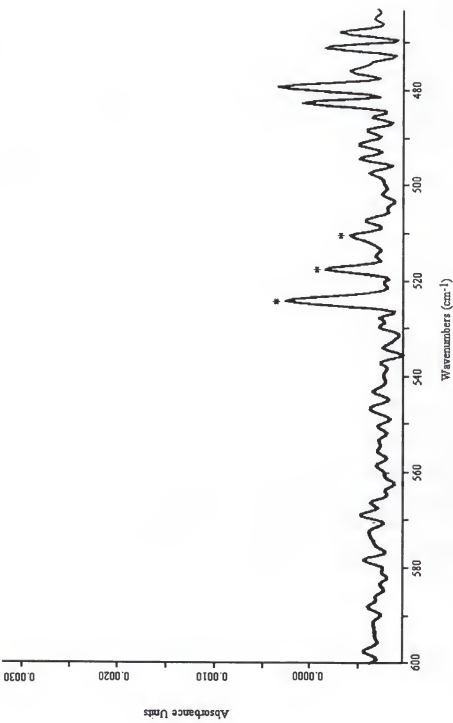


Figure 4.4. The three sites of the ν_3 bending mode of NbO_2 .

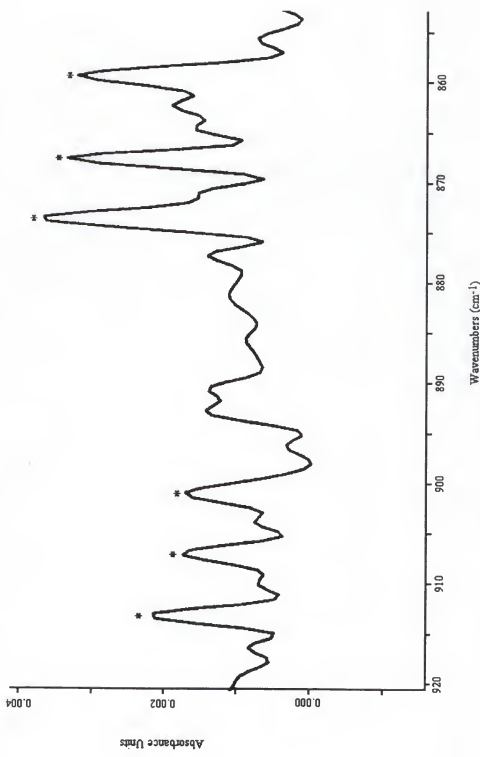


Figure 4.5. The sites of the ν_1 and ν_3 stretching modes of NbO_2 .

electron diffraction study performed by Spiridonov et al.⁴⁰ They reported based on the refinement of their data with ν_3 fixed at 1009 cm⁻¹ that ν_1 and ν_2 were 854(41) and 527(41) cm⁻¹ respectively. The values reported here are well within the error limits given in the above study. Admittedly, they indicate that their treatment is very sensitive to temperature, thus the reported vibrational frequencies have a parametric dependence on temperature with a generous range of error 2678(39) K. In any event, the vibrational frequencies determined in this experiment should give a clearer picture of the true frequencies regardless of subtle matrix effects.

Conclusion

The experiment performed in krypton gives the best evidence that Nb¹²C and Nb¹³C were indeed synthesized. The isotopic shift in frequency of Nb¹³C ($\Delta G''_{1/2} = 908.$, cm⁻¹) relative to Nb¹²C ($\Delta G''_{1/2} = 941.$ cm⁻¹) is quite satisfactory in comparison to a calculated harmonic prediction ($\Delta G''_{1/2} = 908.$ cm⁻¹). The krypton spectra (Figure 4.1) clearly shows these isotopomers with very little interference from impurities. The frequency of Nb¹²C in the krypton matrix ($\Delta G''_{1/2} = 941.$ cm⁻¹) has been substantially reduced as compared to the gas phase value reported by Simard²⁸ ($\Delta G''_{1/2} = 980 \pm 15$ cm⁻¹). The percent shift relative to the gas phase value is 3.9%. This is not atypical, as trapped species in more polarizable matrices tend to have higher shifts relative to the gas phase.³⁰ A comparison of other highly ionic species that have been trapped in matrices shows that, for instance, LiF (dipole moment, $\mu = 6.33$ D) has a shift in a krypton matrix of 6.9% relative to its gas phase value.^{30,31} This would further validate the approximate magnitude of the dipole moment that was calculated by Simard²⁸ ($\mu = 6.06$ D).

The argon spectra (Figure 4.2) seem to exhibit bands of Nb¹²C and Nb¹³C, but are complicated by impurity peaks essentially due to NbO and NbO₂. The isotopic shift in frequency of Nb¹³C ($\Delta G''_{1/2} = 917.\text{7 cm}^{-1}$) relative to Nb¹²C ($\Delta G''_{1/2} = 952.\text{2 cm}^{-1}$) is again quite good compared to the calculated harmonic prediction ($\Delta G''_{1/2} = 919.\text{0 cm}^{-1}$). The percent shift of Nb¹²C relative to the gas phase value is 2.8%.

The neon spectra (Figure 4.3) was the most speculative in terms of definitely assigning bands to Nb¹²C and Nb¹³C, which was discussed earlier. The bands that were assigned to Nb¹³C ($\Delta G''_{1/2} = 949.\text{7 cm}^{-1}$) and Nb¹²C ($\Delta G''_{1/2} = 982.\text{0 cm}^{-1}$) agrees well with the isotopic frequency compared to the calculated harmonic value ($\Delta G''_{1/2} = 947.\text{8 cm}^{-1}$). The percent shift of Nb¹²C relative to the gas phase value is -0.2%. This percentage is not surprising since neon is the least perturbing matrix of the rare gases and most closely resembles gas phase conditions.³⁰

CHAPTER 5 DENSIMETER

Introduction

A complete understanding of the world that we “see” relies on the ability to measure the behavior of a single atom as an isolated entity, as well as the collective behavior of various ensembles of atoms and molecules that are placed under varied environmental scenarios. Ongoing technological advances have enabled scientists to actively research these extreme disciplines. For example, the ability to detect and manipulate a single atom/molecule has recently been reported by several groups.^{41,42} At the other extreme, condensed phase physicists have recently discovered the existence of the Bose-Einstein condensate, predicted by Einstein nearly 70 years ago.⁴³

The unusual behavior of a bulk state is not necessarily confined to the exotic conditions of a Bose-Einstein condensate, but can also be realized in conditions of normal fluids and mixtures that are far removed from the ambient. This behavior is particularly evident near the critical point (P_c , ρ_c , T_c), due to time-dependent fluctuations in density.⁴⁴ As a result, these regions of a phase diagram can be difficult to define thermodynamically due to deficiencies in thermophysical measurements. It has been pointed out by Wagner²⁰ that “the IUPAC Thermodynamic Tables Project Centre at Imperial College London is committed to revise its tables on carbon dioxide,⁴⁵ because the equation of

state used for establishing those tables show quite large systematic deviations from the experimental (p , ρ , T) and caloric values, especially along the coexistence curve and in the critical region.²⁰ Thus, the need for reliable equations of state within the experimental uncertainty of physical measurements is needed.

Furthermore, with the peaking interest of supercritical mixtures as a media for novel chemical activity, the ability to predict the behavior of supercritical mixtures from the complete and accurate thermodynamic surface of the media of interest is tantamount to the complete exploitation of this area. These sentiments have been elucidated in the literature by Poliakoff:⁴⁶ "...reaction mixtures have to be homogeneous in order to exploit the advantages of supercritical fluids. Therefore, a knowledge of their phase envelopes and critical points is crucial. Even the simplest reaction system will be a ternary mixture (reaction, product, and solvent)... and traditional methods of phase measurements (view-cell or sampling) are often very difficult to apply to some ternary mixtures where the density differences are small."⁴⁶

The reoccurring theme of these observations, as stated in the literature, is the ability to measure the state variables (i.e., p , ρ , and T) very accurately and with the utmost precision. The state-of-the-art techniques for these measurements are adequate for temperature and pressure, but density determinations are non-trivial, especially if a system is well removed from the ambient. But, why is density so important?

Thermodynamic Relationships

The ability to control the behavior of bulk chemical systems involves using the predictive power of a thermodynamic equation of state that is developed based on the

physical property measurements of these aforementioned independent variables. If these variables are satisfactorily measured, all of the other thermodynamic properties of a fluid can be expressed in terms of the Gibbs energy $G(T,P)$ or in terms of the Helmholtz energy $A(T,\rho)$. It has been pointed out previously⁴⁷ that for regions of low or moderate pressures, either set of variables is fully satisfactory. However, when the two-phase, vapor-liquid region is involved, the Helmholtz energy (A) is much more satisfactory since it is a single valued function of T and ρ . This results from the density (ρ) being a multi-valued function of temperature and pressure in this region of the phase diagram. It is possible to tabulate or write separate equations for vapor and liquid properties in terms of the Gibbs energy (G) (as functions of temperature and pressure) but, if one wishes a single comprehensive equation of state, one uses T and ρ as variables and the Helmholtz energy (A) as the parent function.

The parent function in both cases is the sum of two functions, one for the ideal-gas or standard-state properties and the other for the departure of the fluid from ideal behavior. Equations 81 and 82 show the Helmholtz energy (A) developed in terms of an ideal gas and its relationship to its standard state properties, where $\rho^0 = P^0/RT$ ($P^0 = 1$ bar) and $G^0 = A^0 + RT$. The departure of the Helmholtz energy from the ideal case is related by the following equations (83 and 84), where the compression factor z is defined as $V_m = zRT/P'$ and $P' = \rho'RT$.

$$A^{id}(T, \rho) - A^0(T) = RT \ln(\rho / \rho^0) \quad (81)$$

$$= G^0(T) + RT[-1 + \ln(\rho RT)] \quad (82)$$

$$\left[\frac{\partial(A - A^{id})}{\partial p} \right]_T = V RT - RT / p \quad (83)$$

$$A(T, p) - A^{id}(T, p) = RT \int_0^p (z - 1) d \ln p' \quad (84)$$

As an aside, it should be mentioned that the development of an equation of state is often given for the Helmholtz energy (A) instead of a compression factor (z), where one first divides A into an ideal and a residual term (Equation 85). The compression

$$A = A^{id} + A^{res} \quad (85)$$

factor is then defined in terms of a residual Helmholtz energy (A^{res}). But, if the compression factor is initially defined as was the case here, the residual Helmholtz equation (A^{res}) is defined in equation 86, which essentially represents the departure of the Helmholtz energy (A) from the ideal case (A^{id}). The final equation for the Helmholtz energy is therefore equation 87. Substituting an appropriate equation of state for the

$$A^{res} / RT = \int_0^p (z - 1) d \ln p' \quad (86)$$

$$A(T, p) = G^0(T) + RT[-1 + \ln(pRT)] + A^{res} \quad (87)$$

compression factor ($z-1$) developed in terms of density, (the virial equation for example) gives the complete Helmholtz energy (88), which can be utilized to derive most of the other thermodynamic relationships.

$$A(T, \rho) = G^0(T) + RT[-1 + \ln(\rho RT) + B\rho + C\rho^2 + \dots] \quad (88)$$

It is obvious that a nearly complete thermodynamic description of a normal fluid can be obtained with the above relationships, but they are contingent on the accurate and precise measurement of the state variables with density as the most elusive. With these points in mind, the goal at the outset was the development of an all encompassing density measuring instrument with the following criteria: 1) accuracy/precision, 2) sensitivity, 3) robustness, and 4) self-calibrating abilities (as an enhanced feature). Thus, the focus of this study was the development of a state-of-the-art Archimedes type densimeter that in principle would measure fluid densities over a wide range of temperatures and pressures.

First Principles

An Archimedes type densimeter relies on principles developed around 200 B.C.⁴⁸ by one of the greatest scientists of antiquity, Archimedes. These principles are based on the buoyancy force that is subjected to objects submerged in a fluid. For instance, the forces that act on a rigid body that is immersed in a static, isothermal fluid are: 1) Newton's second law of motion and 2) the buoyancy force (see Figure 5.1). The former is the gravitational force (equation 89), where \vec{F}_g is Newton's force of gravity, m is the mass of the object, g is the acceleration of gravity, and \vec{n} is a unit vector directed along the center of the masses of the two bodies. The latter force (\vec{F}_b) (equation 90) is

$$\vec{F}_g = mg\vec{n} \quad (89)$$

dependent on the density (ρ) of the medium and the volume (V) of the fluid displaced by

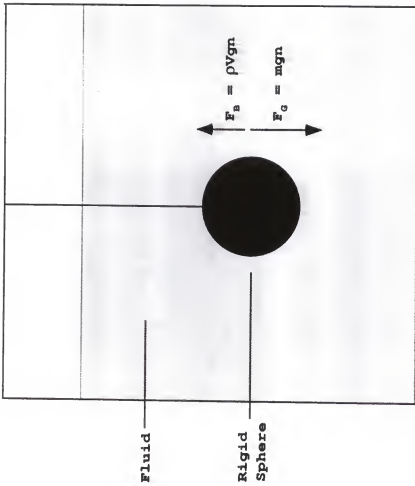


Figure 5.1. A schematic of the gravity and buoyancy forces on a sphere immersed in a static fluid.

the object. The local acceleration of gravity (g) and \bar{n} are defined as they were in the previous equation. These two forces act in opposition, and thus the resultant force

$$\bar{F}_B = \rho V g \bar{n} \quad (90)$$

experienced by the immersed object is the intrinsic weight (\bar{F}_g) less the buoyancy

$$\bar{F}_g = (\rho g - \rho V g) \bar{n} \quad (91)$$

force (\bar{F}_g) (see equation 91). It is now evident that in principle it is possible to solve for

the density of an unknown fluid if the force of a submerged mass could be measured.

Design of Densimeter

The ability to measure the density of an object under ambient conditions is a relatively simple matter. But, the sampling of density far removed from ambient conditions is a non-trivial measurement. If one recognizes from equation 91 that the density can be ascertained from the knowledge of the net force applied to an object in a fluid, a density measurement would ostensibly be feasible. But, the net force on an enclosed object under extreme pressures and temperatures is a very difficult measurement. To begin to mitigate this problem, a spring can be used to suspend the body within the fluid. Consequently, the force applied by the rigid body can be related to the spring's displaced position. If the spring obeys Hooke's Law (which is an excellent approximation over a very short deflection range), the deflection will be linearly

dependent on the total or net force placed upon the system (equation 92). In this expression, k is the force constant of the spring and \bar{x} is the displacement of the spring from its equilibrium position.

$$\bar{F} = -kx\bar{n} \quad (92)$$

If we consider the suspension of a sphere from a spring that has been described above, the net force experienced by an individual sphere is now incident on the spring and causes an expansion that is characteristic of the resultant load (equation 93). In this

$$\bar{F}_{\text{net}} = (mg - \rho V g)\bar{n} = -kx\bar{n} \quad (93)$$

experiment, two rigid spheres (with masses m_1 and m_2 and respective volumes V_1 and V_2) were placed in a rack and suspended from a spring in a static, isothermal fluid (see Figure 5.2). With this arrangement, it is possible to measure the force (specifically the position) of four separate loads. Four linear equations are the result of the above measurement of position as a function of the fluid's density (see equations 94 - 97). The displaced

$$\bar{F}_0 = (m_0g - \rho V_0g)\bar{n} = -kx_0\bar{n} \quad (94)$$

$$\bar{F}_1 = (m_1g - \rho V_1g + m_0g - \rho V_0g)\bar{n} = -kx_1\bar{n} \quad (95)$$

$$\bar{F}_2 = (m_2g - \rho V_2g + m_0g - \rho V_0g)\bar{n} = -kx_2\bar{n} \quad (96)$$

$$\bar{F}_3 = (m_3g - \rho V_3g + m_0g - \rho V_0g)\bar{n} = -kx_3\bar{n} \quad (97)$$

position of the spring due to the net force of each loading was monitored by a commercially available linear variable differential transformer (LVDT), which transduced

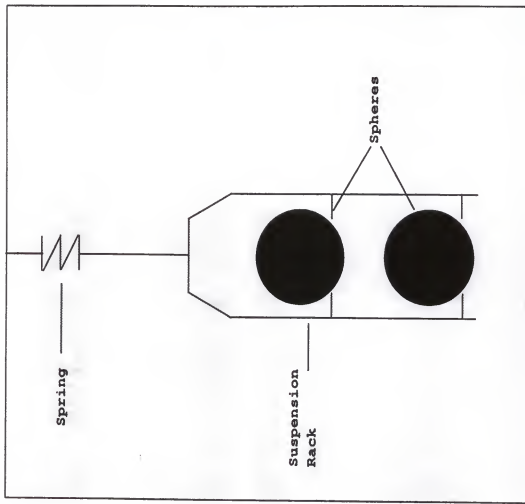


Figure 5.2. A schematic of spheres and a rack suspended from a spring.

the displacement to a voltage. The resultant equations that were used to solve for density are represented below (equations 98 - 100), where S is the signal in terms of voltage and K is the linear conversion of effective mass to voltage (At the outset, this constant is assumed completely linear over the deflection range of interest.). The fourth measurement (see equations 94-97) is a linear combination of the other three, thus there

$$\bar{F}_0 = (m_0g - \rho V_0 g)\bar{n} = -kx_0\bar{n} = S_0 K(x) \quad (98)$$

$$\bar{F}_1 = (m_1g - \rho V_1 g + m_0g - \rho V_0 g)\bar{n} = -kx_1\bar{n} = S_1 K(x) \quad (99)$$

$$\bar{F}_2 = (m_2g - \rho V_2 g + m_0g - \rho V_0 g)\bar{n} = -kx_2\bar{n} = S_2 K(x) \quad (100)$$

are only three resultant equations with three unknowns ($(m_0 - \rho V_0)$, Kg/k , and ρ), which can be solved to ascertain density. Note that the scaling constants (Kg/k) in these equations are grouped together as one term.

The elegance of this particular design allows for the determination of the density without the explicit knowledge of the local acceleration of gravity (g), the force constant of the spring (k), or the LVDT constant (K). For example, the spring constant of the material will vary with temperature and pressure, but it will not vary over a single density measurement. Secondly, the local acceleration of gravity (g) should vary negligibly over the distances (0.100") in this experiment. And, it assumed that a linear response will be provided by the LVDT. *Therefore, these constants cancel out of the resultant system of equations when they are solved. And, in theory, the instrument is a self-calibrating device.*

Densimeter Development

To bring to experimental fruition the highly attractive theoretical features of this type of densimeter, an arduous trial and error procedure ensued. The critical component and ultimately the foundation of this instrument was the sensing device that measured the uniaxial displacement of the spring with a resultant load. As was mentioned in the previous section, an extremely short deflection range was needed to ensure the linearity of the deflected spring. Thus a sensing device was needed that had the combination of a reasonably short stroke coupled with a high resolution of linear displacement. Therefore, an LVDT (Linear Variable Differential Transformer) sensing device (Trans-Tek, Inc. model #240-0015) was purchased with a deflection range of 0.100" and a resolution of ± 1 micron. The constituent parts of an LVDT consist of a weakly magnetic core (0.99" OD X 0.492") and a cylindrical transformer with a cored center. The position of the magnetic core relative to the transformer of the LVDT gives a linear voltage response when it is displaced from a null position (a voltage of zero) to ± 6 volts corresponding to $\pm 0.50"$ displaced distance.

With the desired specifications of the LVDT in hand, the next most important aspect of the design and engineering process was to find a spring material that would lend itself to the rigors of this experiment and more importantly have an extremely elastic behavior over wide ranges of pressures and temperatures. In addition, the spring would have a deflection of approximately 0.080" with a given load to take advantage of the maximum stroke of the LVDT. The spring material that was chosen for use in this apparatus was fused quartz. Quartz was chosen because of its extremely elastic behavior

under environmental stresses ($\alpha = 5.5e-7 \text{ cm cm}^{-1} \text{ }^{\circ}\text{C}^{-1}$),⁴⁹ and its resistance to hysteresis when a load is placed on it over time (due to its amorphous structure). A stock piece of fused quartz (0.06" OD) was heated, wound around a mandrel and placed in a lathe to generate a coiled spring with the approximate dimensions of 0.25" OD and 0.5" Length. Excellent control of the spring constant could be exercised with bench top measurements of deflection by etching the quartz (2.5 M) over carefully monitored time periods to obtain the desired deflection of approximately 0.80" with a load of 25g.

From a previous design of another densimeter model,⁵⁰ two hollow stainless steel spheres were fabricated and used as a changeable load that was to be placed on a rack. In the current design, the rack and the spheres would then be suspended from a spring and the displacement sensed by the LVDT. The sinkers were originally designed to have approximately the same volume ($V_1=V_2$), but one sinker would have twice the mass ($2m_1=m_2$). They were machined from hemispheres made of 304 stainless steel with a 0.625"OD and a 0.437" ID, which gave a sufficient wall thickness to prevent any dimensional change (and therefore volume change) up to 3000 psia. A copper bead that had the mass of two hemispheres was placed in one set of hemispheres (to achieve approximately twice the mass of the other), and the two sets of hemispheres were then Heli-Arc welded at the seam. The masses and volumes of the spheres were determined via an analytical balance and pycnometric volume determinations.⁵⁰

The remaining parts of the densimeter were built around the specifications of these integral components. To begin with, a rack to hold the buoys was fabricated to

suspend from the quartz spring. The rack was designed to incorporate the LVDT magnetic core into a suspension post that screwed into the rack so as to make a single unit (see Figure 5.3 for schematic). This rack was assembled by brazing two 0.062" diameter stainless steel rods onto a brass disc. The actual supports for the spheres were short pieces of stainless steel wire that were brazed in a V-shape to these rods. The brass disc was drilled an tapped 5-40. Two brass posts were then fabricated to connect the brass disc to the quartz spring, and linked between them was the magnetic core of the LVDT. The first rod was threaded 5-40 on one end to place into the brass disc, and the other end was threaded 1-72 to place into the LVDT magnetic core. The second brass rod had a small hole drilled in the center of a small flattened section to accommodate a hook that extended from the quartz spring to link the rack to the spring. And, finally the other end of this second rod was threaded 1-72 on one end (to place into the other end of the magnetic core).

With the rack unit in place, there was the need to independently lift the buoys from the rack. Mechanical lifters were designed to fit into a cylindrical, brass sleeve (1.049" OD), which in turn would slip fit around the rack and spheres. Vertical slides were dimensioned to provide proper clearance for each individual loading so as to prevent any mechanical contact between the rack and the sleeve and to ensure that the load would hang freely from the spring. The lifters were actuated via a magnetically coupled cam system that lifted the spheres from the rack to provide the instrument with four independent loads.

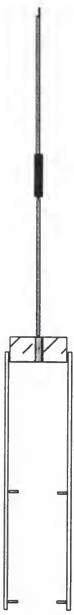


Figure 5.3. A schematic of the LVDT core mounted between two brass posts.

The aforementioned brass sleeve (Figures 5.4 - 5.9) was machined with two slots that were 90° apart to accommodate the lifter slides. These slides were made from brass ($3.990'' \times 0.185'' \times 0.145''$) and were fitted with stainless steel forks ($1/32''$ diameter) that were brazed into the body of the lifter slides. The forks had three points that provided support for spheres when lifted from the rack. Finally, the lifter slides were slotted at the bottom and fitted with small brass wheels to ride on the cam assembly to actuate the motion of the lifter slides (see Figure 5.10). The magnetically driven cam assembly (Figure 5.11) is a two-tier cam equipped with an internal magnet, which is coupled to an external magnet. The cam has a 45° step with a total rise of $0.250''$. The quadrants of the cam allow for the motion of the lifters to give four separate loads referred to earlier. The cam is fitted onto a magnetic turner (Figure 5.12) by a stem that locked into position by a set screw. The cam rides on brass ball bearings (Figure 5.13) placed in between the cam and the magnetic holder. In turn, the cam and magnetic turner unit rotates on a set of brass ball bearings that sets on the bottom of the densimeter can. A ferromagnet was placed into a drilled out section of the magnetic turner, which was held in place with a set screw. The ferromagnet was coupled to an external magnet that drove the cam assembly.

At this point, the densimeter was assembled into two main components (see Figure 5.14 for schematic assembly drawing). The upper component consisted of the following pieces: 1) a top flange (Figure 5.15) equipped with a brazed spring mount, a ball bearing support clamp for a drive screw (see Figure 5.16), a drive screw (Figure 5.17) that actuated the movement of the LVDT housing (Figure 5.18 and 5.19), and a top

flange cover (Figure 5.20). 2) a bottom flange (Figure 5.21) that was married to a complimentary flange on the densimeter body and supported the top flange via support legs (Figure 5.22). The top and bottom flanges were physically joined by an inconelTM sleeve (see Figure 5.23) that traversed the LVDT housing and encompassed the LVDT core.

The lower component was made up of a densimeter body (Figure 5.24) that contained an end cap (Figure 5.25) brazed into the bottom, a magnetic turning unit, and a cam assembly. A flange (shown in Figure 5.24) was brazed onto the densimeter body (complimentary to the bottom flange) in order to marry the two components together and create a high pressure seal. This seal utilized a copper gasket that was fabricated by cutting a piece of 12 gage copper wire to a length of 3.92", and the ends Heli-Arc welded together to make a continuous piece. The copper gasket was implemented by initially placing it around the diameter of the densimeter body and resting it on the offset of the bottom flange. The upper was then placed on top of the bottom flange and the twelve 10-32 bolts were tightened to compress the copper wire into the gland between the two flanges. The gasket is dimensioned to fill 95% to 98% of the triangular cross-sectional area of the gland.

Experimental

To initially test the viability of this instrument; temperature, pressure, and density data for argon and carbon dioxide were acquired over several isotherms near ambient temperature, but over a wide range of pressures and thus density. These tests would bring

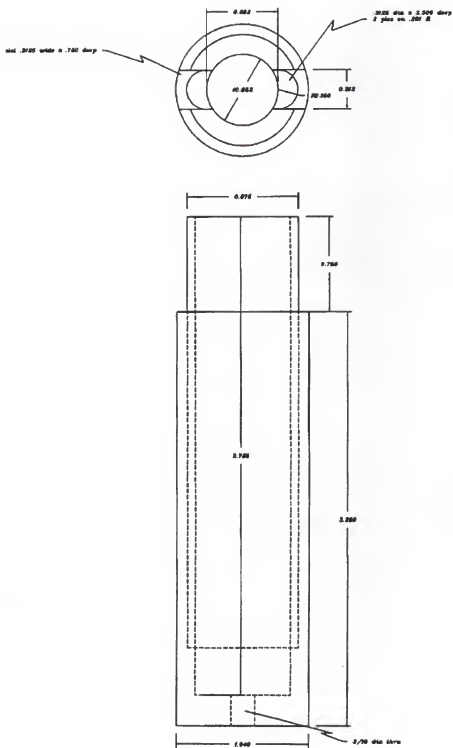


Figure 5.4. The cut-away view of the brass sleeve.

12:00 and 6:00 position

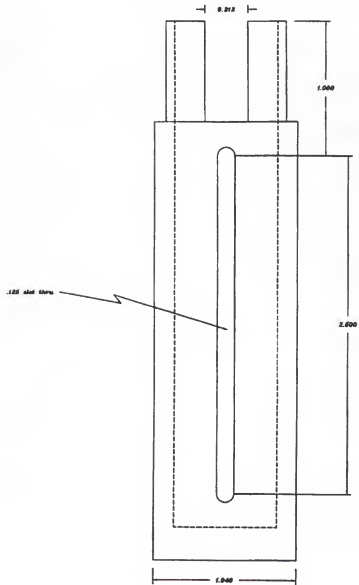


Figure 5.5. The 12:00 and 6:00 position of the brass sleeve.

12:00 POSITION

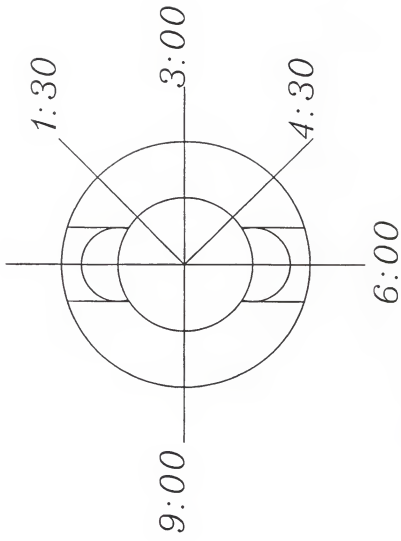


Figure 5.6. The respective positions of the brass sleeve.

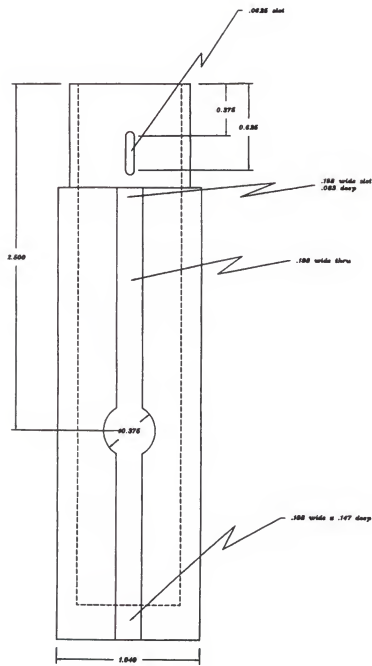
1:30 position

Figure 5.7. The 1:30 position of the brass sleeve.

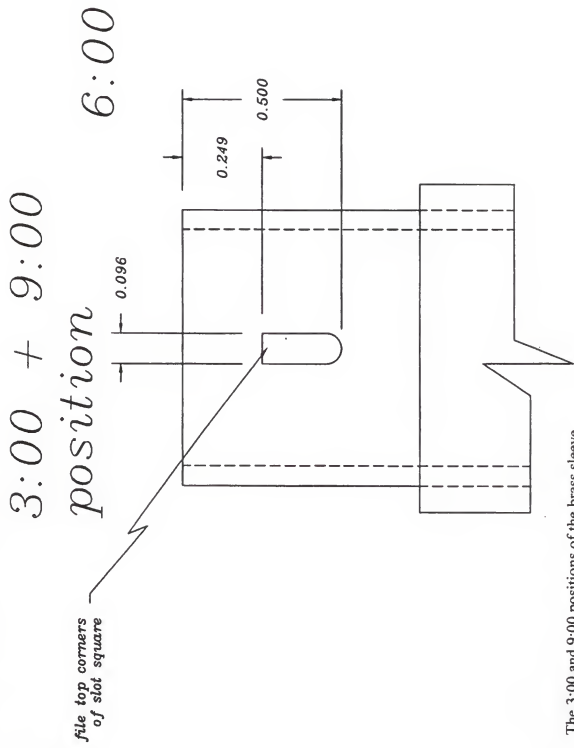


Figure 5.8. The 3:00 and 9:00 positions of the brass sleeve.

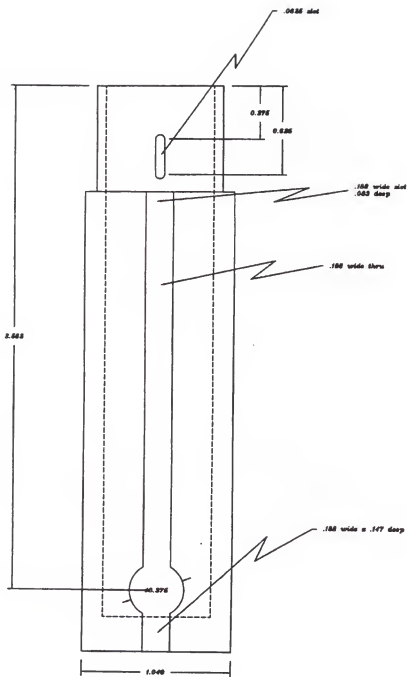
4:30 position

Figure 5.9. The 4:30 position of the brass sleeve.

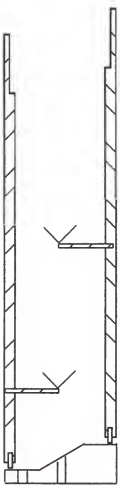
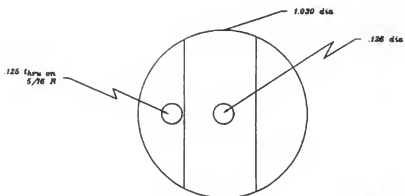


Figure 5.10. A schematic of the lifter slides actuated by the motion of a cam.

cam



*MATL.
SS*

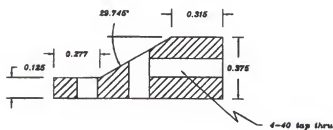
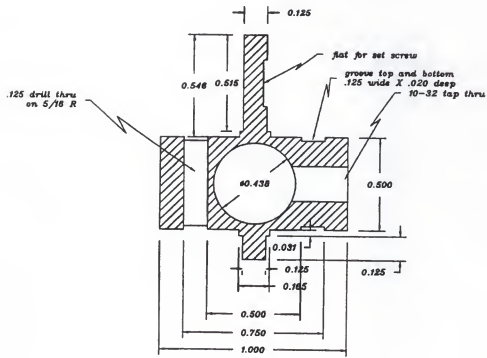


Figure 5.11. The cut-away and top view of the cam.

magnet holder



MATL. BRASS

Figure 5.12. The cut-away and top view of the magnet holder.

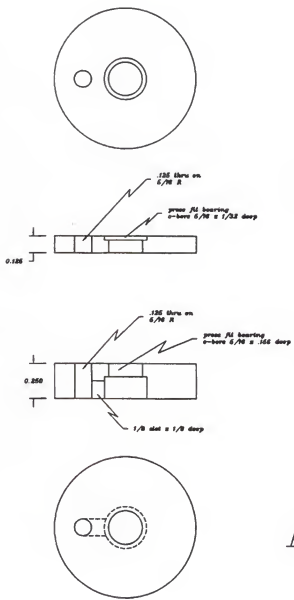
shims

Figure 5.13. The cut-away and top view of the brass shims.

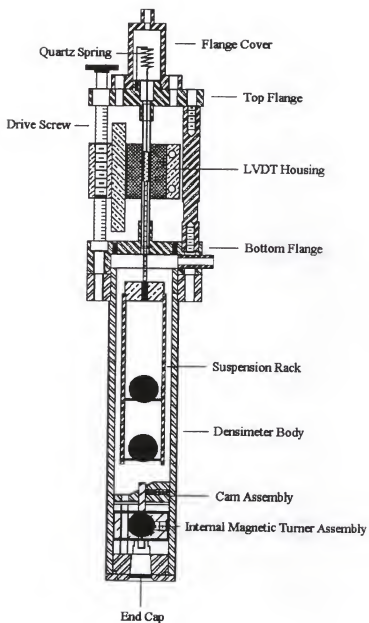
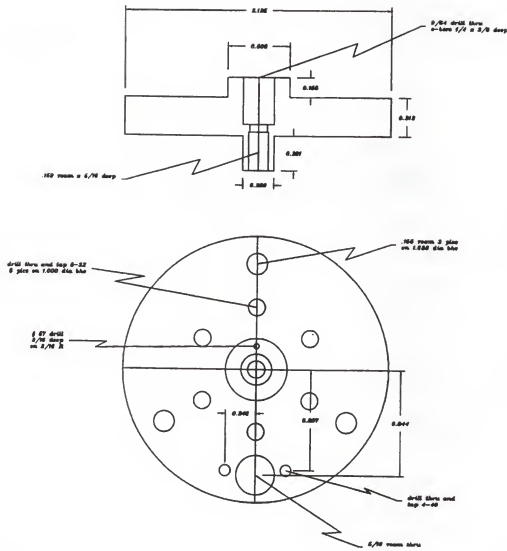


Figure 5.14. The assembly drawing of the densimeter.

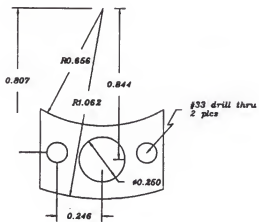
top flange



matl. ss

Figure 5.15. The cut-away and top view of the top flange.

support clamp



*matl. brass
3/32 thk*

Figure 5.16. The support clamp that is mounted on the top flange.

drive screw

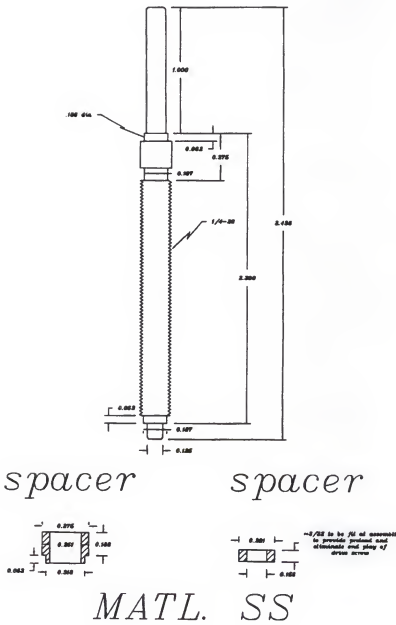
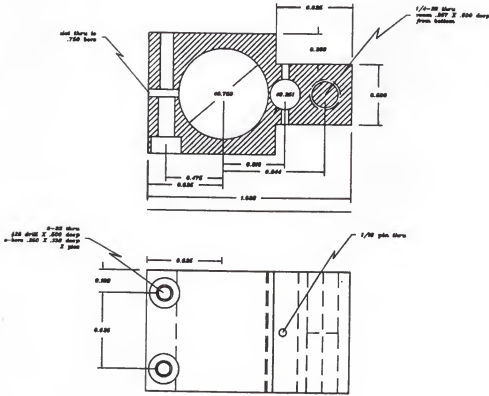


Figure 5.17. The drive screw assembly.

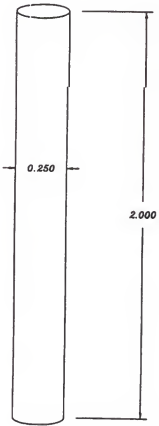
coil holder



MATL. BRASS

Figure 5.18. The cut-away and side view of the coil holder.

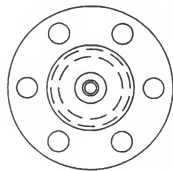
stop pin



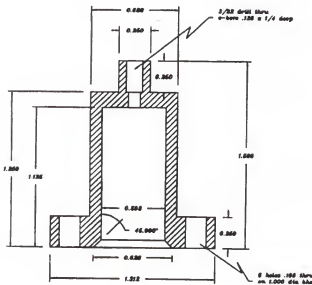
MATL. SS

Figure 5.19. The stop pin that is mounted in the LVDT housing.

cover flange
top



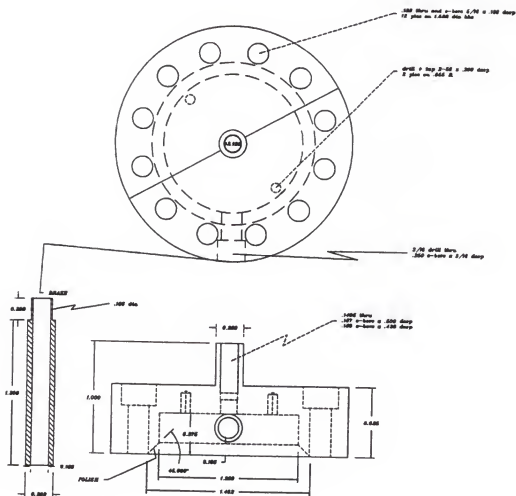
side



MATL. SS

Figure 5.20. The cut-away and top view of the top flange cover.

BOTTOM FLANGE



MATL. SS

Figure 5.21. The cut-away and top view of the bottom flange.

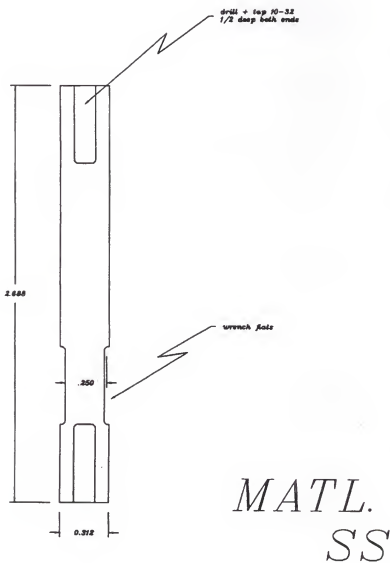
support legs

Figure 5.22. The support legs mounted between the top and bottom flanges.

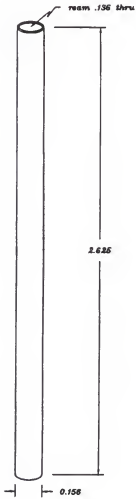
magnet sleeve*matl. inconel*

Figure 5.23. The inconel magnet sleeve brazed between the flanges.

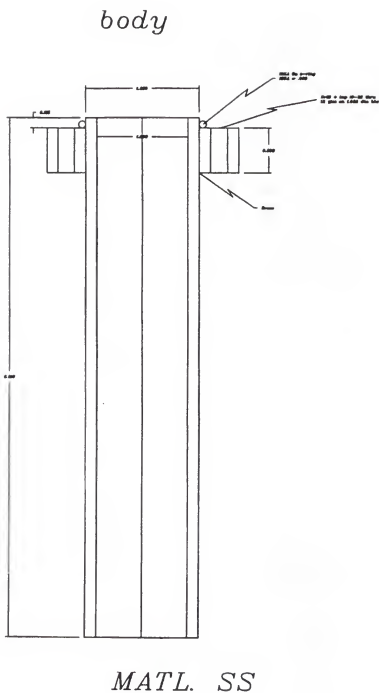


Figure 5.24. The densimeter body.

END CAP

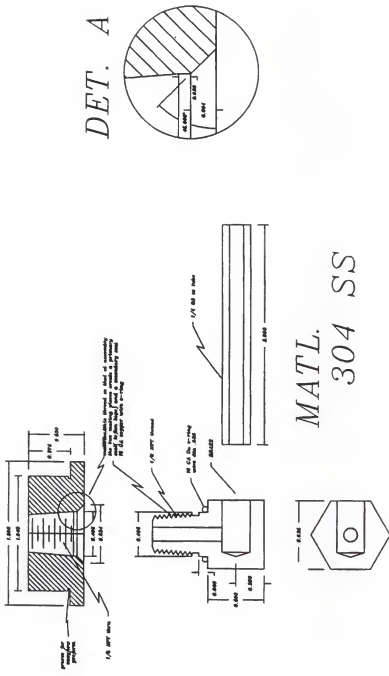


Figure 5.25. The end cap placed in the bottom of the densimeter body.

to bear the overall operational ability of this prototype instrument and allow for any design modifications that would need to be undertaken.

As mentioned previously, in order to obtain nearly complete bulk thermodynamic information, density along with temperature and pressure need to be sampled concurrently. In these experiments, the densimeter was coupled with state-of-the-art pressure and temperature measuring devices. A Sensotec model TJE/743-03 strain gage pressure transducer was used in conjunction with a Beckman model 610 electronic readout to display and sample the pressure data. The Sensotec transducer was calibrated with a Ruska (model 2465) standardized dead weight pressure gage. The temperature was monitored with a four wire platinum RTD (resistance temperature device) interfaced to a Keithley digital multimeter (model K-196). This RTD was calibrated versus a standard RTD (HY-CAL engineering, N.I.S.T. traceable). The block diagram in Figure 5.26 shows the schematic setup for the densimeter and the ancillary components. The densimeter, pressure transducer, and the RTD are enclosed in an insulated temperature controlled oven equipped with six circulating fans that was retrofitted with a newly developed liquid nitrogen refrigeration control valve (see reference 50 for details). A PID control algorithm monitored the valve and provided temperature control to ± 0.01 mK. All of the above mentioned devices were interfaced to a personal computer (486 internal processor operating at 33 MHz with 16 megabytes of RAM) via the standardized IEEE general purpose interface bus (GPIB) (see Figure 5.26).

The actual data collection procedure followed the following protocol: 1) The densimeter along with the ancillary components (RTD, pressure transducer and the

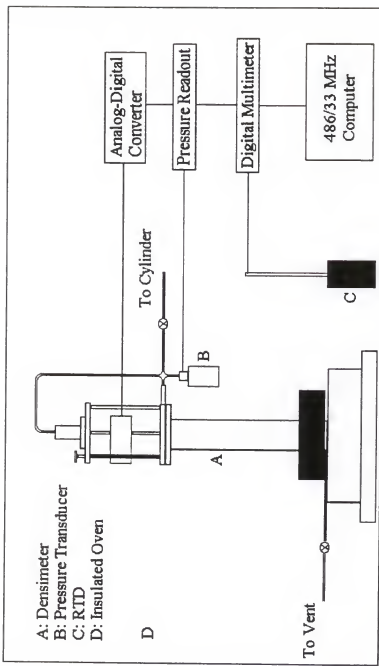


Figure 5.26. The block diagram of the hardware and electronics of the densimeter.

accompanying connective hardware) that were contained within the insulated oven were first charged to approximately 100 psia with the gas of interest. A vacuum was then applied to remove the gas and any lingering gaseous contaminants, and this procedure was repeated several times to ensure that impurities were driven from the system. 2) After the system was charged to the desired pressure, the oven was started. The oven generated heat from the operation of the fans that was countered by the actuation of a PID controlled liquid nitrogen valve (previously mentioned) interfaced to the personal computer. A desired temperature setpoint was entered into the PID algorithm and equilibration of the desired temperature (± 10 mK) was obtained within 2-3 hours. 3) After the equilibration time, the magnetically driven cam assembly of the densimeter was manually turned to a position that corresponded to a specific load. The displacement of the quartz spring due to the effective load (corresponding to the competing forces due to mass and density) was linearly transduced to a voltage by the LVDT and its circuitry. The voltage was acquired with an Iotech model ADC488/8SA analog to digital converter (ADC) that sampled the voltage at a rate of 1kHz. The final voltage then for this particular reading was an average of 16,384 voltage readings averaged over 16.4 seconds. During this acquisition, the temperature was acquired by sampling the resistance of the RTD from the Keithley model K-196 digital multimeter. The pressure was sampled simultaneously from a Beckman model 610 electronic readout used in conjunction with the Sensotec model TJE/743-03 strain gage pressure transducer. The cam assembly was turned to a new position (a new effective load) and the above procedure was repeated.

until all four loads were sampled. The acquisition of four loads consisted of one trial. A minimum of ten trials were obtained for this particular pressure, temperature, and density.

Several runs were obtained along the same isotherm, corresponding to different densities. This was accomplished by bleeding the system of some fluid to obtain a new density. Thus, the P,T, ρ surface was obtained by reloading the system with a suitable density and sampling at different isotherms.

Results

Argon

Argon (Bitec, 99.99% purity) was chosen to initially test the viability of the densimeter, because of its nearly ideal behavior over the temperature and pressure regions selected for the testing. The pressure range for the tests were from approximately 550 psia to 1750 psia at temperatures of 278.15K, 288.15K, and 298.15K. This corresponded to a density range of approximately 70 kg/m^3 to 210 kg/m^3 . Table 5.1 shows the density data collected over this region for Argon. The density data reveals a $\pm 2.76 \text{ kg/m}^3$ average standard deviation of the density over these temperature and pressure ranges compared to a truncated virial equation of state (ref. American Institute of Physics Handbook). This data is compared graphically in Figure 5.27. The data shows the operational accuracy of this instrument to be within at worst 1% relative standard

Carbon dioxide

Carbon dioxide (Scott Specialty Gases, 99.999% purity) was chosen as a more typical, non-ideal system to test the performance of the densimeter over a broader range

temperatures. The P,T, and ρ data is represented in Table 5.2. The standard deviation is $\pm 10.9 \text{ kg/m}^3$ compared to densities calculated via a Redlich-Kwong equation of state that was generated with the experimental data (see reference 11). The data in Table 5.2 is graphically represented in Figure 5.28. Again, for the carbon dioxide data an upper limit seems to be approximately 1% for the relative standard deviation.

Conclusion

In general, the relative standard deviation that is reported for the above data would not be acceptable as an upper limit for operation, but this densimeter at the outset is designed for high pressure, non-ideal fluids where equations of state cannot begin to predict accurately the densities of these surface regions. Furthermore, the experimental relative standard deviations should decrease at higher densities if this indeed is a systematic deviation.

The densities that were sampled over these temperature and pressure ranges were generally in agreement with the standard equations of state that were chosen for comparison. Experimentally, what did not compare favorably were the density values as the temperature deviated further from the ambient. It was apparent that the response of the LVDT was the source of error. It was reasoned that the LVDT transformer was optimized for linearity at or near ambient temperatures (although operational range of the LVDT was given to be 220 K - 394 K), because there was an attempt to thermostat LVDT and the result was a much better agreement of density data. Thus, the obstacle with the current design of the instrument is the response of the LVDT as the temperature

Table 5.1. Experimental argon (39.948 g/mol) densities compared to Virial EOS densities.

T (K) \pm 0.01	P (psia) \pm 0.5	ρ_{exp} (kg/m ³) \pm 2.76 _{SD}	ρ_{virial} (kg/m ³)
278.15	563.6	69.29	69.66
	753.7	94.22	94.36
	858.5	107.3	108.2
	1016.8	128.2	129.6
	1208.3	153.3	156.1
	1359.7	172.8	177.6
	1417.4	183.0	185.8
	1544.5	198.8	204.2
288.15	581.6	68.55	69.05
	740.7	88.70	88.75
	887.2	106.3	107.2
	995.3	120.5	121.0
	1000.8	120.7	121.7
	1150.0	138.6	141.0
	1253.2	151.2	154.6
	1270.0	154.1	156.9
	1416.7	174.0	176.5
	1471.3	181.2	183.7
	1671.9	205.1	211.4
298.15	578.4	66.10	65.95
	731.0	83.47	83.96
	864.9	99.65	99.96
	1014.1	117.2	118.0
	1166.1	135.0	136.6
	1304.5	151.8	153.9
	1312.7	152.4	154.9
	1412.0	164.0	167.4
	1444.4	169.7	171.5
	1614.5	189.4	193.2
	1755.8	208.3	211.5

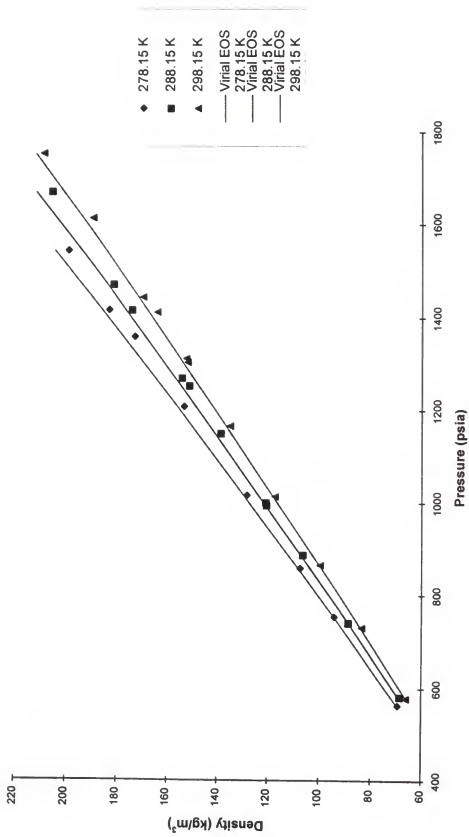


Figure 5.27. The experimental argon density data versus calculated densities (Virial EOS).

Table 5.2 Experimental carbon dioxide (44.011 g/mol) densities compared to Redlich-Kwong calculated densities.

T (K) \pm 0.01	P (psia) \pm 0.4	ρ_{exp} (kg/m ³) \pm 10.9 _{SD}	ρ_{RK} (kg/m ³) ^a
290.15	1017.5	841.1	830.3
	1068.8	843.1	837.9
	1127.9	851.7	846.0
	1355.3	868.2	873.1
	1612.4	889.8	898.5
297.15	1048.6	770.6	758.4
	1127.3	783.0	774.5
	1257.5	804.1	798.7
	1401.3	821.1	820.8
	1573.0	839.7	843.0
300.15	1005.5	700.1	-
	1052.8	720.5	-
	1329.8	787.0	780.6
	1581.4	819.0	819.6
	1804.3	836.3	846.6
303.15	1235.4	730.1	723.8
	1500.5	780.7	780.4
	1769.3	814.9	819.6
307.15	1172.2	584.1	618.6
	1219.0	639.1	649.2

^aValues taken from reference 51.

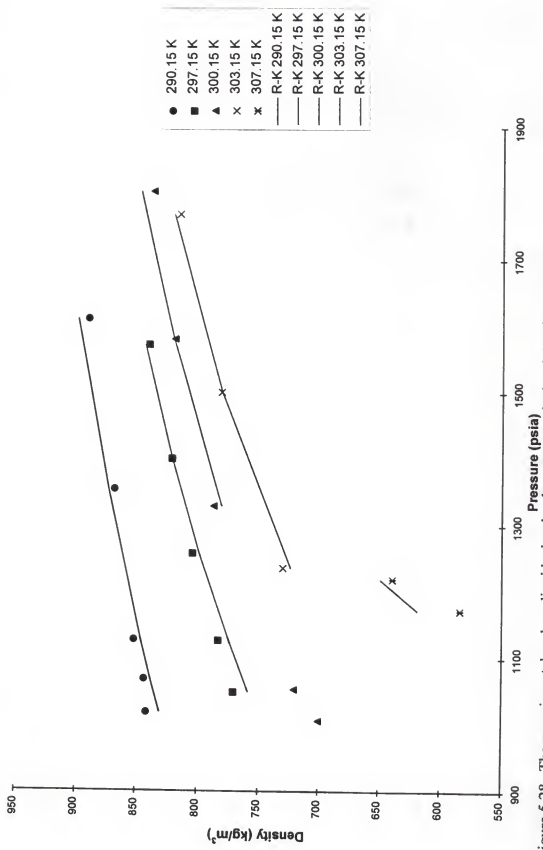


Figure 5.28. The experimental carbon dioxide density data versus calculated densities (R-K).

varies. This could be mitigated via the isolation of the LVDT from the temperature controlled environment or the replacement of the LVDT with a hardier model.

REFERENCES

1. Weltner, W., Jr. *Magnetic Atoms and Molecules*; Dover, New York, 1989.
2. Ramsey, N.F. *Molecular Beams*; Oxford University Press, London, 1956, Chaps. 3 and 9.
3. Weil, J.A. *J. Magn. Reson.* 1971, 4, 394.
4. Kauffman, J.F. *Anal. Chem.* 1996, 248 A.
5. Eckert, C.A.; Knutson, B.L.; and Debenedetti, P.G. *Nature*. 1996, 383, 313.
6. Evilia, R.F.; Robert, J.M.; and Whittenburg, S.L. *J. Phys. Chem.* 1989, 93, 6550.
7. Bowman, L.E.; Palmer, B.J.; Garrett, B.C.; Fulton, J.L.; Yonker, C.R.; Pfund, D.M.; and Wallen, S.L. *J. Phys. Chem.* 1996, 100, 18327.
8. Howdle, S.M. and Bagratashvili, V.N. *Chem. Phys. Lett.* 1993, 214, 215.
9. Chen, S.; Miranda, D.T. and R.F. Evilia, *J. Supercrit. Fluids*. 1995, 8, 255.
10. Betts, T.A.; Zagrobelny, J.; and Bright, F.V. *J. Am. Chem. Soc.* 1992, 114, 8163.
11. Anderton, R.M. and Kauffman, J.F. *J. Phys. Chem.* 1994, 98, 12117.
12. Anderton, R.M. and Kauffman, J.F. *J. Phys. Chem.* 1995, 99, 13759.
13. Heitz, M.P. and Bright, F.V. *J. Phys. Chem.* 1996, 100, 6889.
14. Heitz M.P. and Maroncelli, M.J. *J. Phys. Chem. A.* 1997, 101, 5852.
15. Betts, T.A.; Zagrobelny, J.; and Bright, F.V. *J. Am. Chem. Soc.* 1992, 114, 7821.
16. Randolph, T.W.; O' Brien, J.A.; and Ganapathy, S. *J. Phys. Chem.* 1994, 98, 4173
17. Randolph, T.W. and Carlier, C. *J. Phys. Chem.* 1992, 96, 5146.
18. Batchelor, S.N. *J. Phys. Chem. B.* 1998, 102, 615.

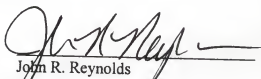
19. de Grazia, J.L.; Randolph, T.W.; and O'Brien, J.A. *J. Phys. Chem. A.* **1998**, 102, 1674.
20. Gilgen, R.; Kleinrahm, R.; and Wagner, W. *J. Chem. Thermodynamics.* **1992**, 24, 1243.
21. Lorentzen, H.L. and Hansen, B.D. *Critical Phenomena*. Green , M.S. and Sengers, J.V. Eds.; Proc. of a Conf., Washington, **1966**, p. 213.
22. Castro, M.D.; Valcarel, M.; and Tena, M.T. *Analytical Supercritical Fluid Extraction*; Springer-Verlag, Berlin, **1994**, Chap. 3.
23. Schneider, D.J. and Freed, J.H. *Biological Magnetic Resonance*; Berliner, L.J. and Reuben, J. Eds.; Plenum Press, New York, **1989**, Vol. 8, p. 1.
24. Libertini, L.J. and Griffith, O.H. *J. Chem. Phys.* **1970**, 53, 1359.
25. Graybeal, J.D. *Molecular Spectroscopy*; McGraw-Hill, New York, **1988**.
26. Bernath, P.F. *Spectra of Atoms and Molecules*; Oxford Press, New York, **1995**.
27. Castleman, A.W., Jr. and Bowen, K.H., Jr. *J. Phys. Chem.* **1996**, 100, 12, 911.
28. Simard, B.; Presunka, P.I.; Loock, H.P.; Berces, A.; and Launila, O. *J. Chem. Phys.* **1997**, 107, 307.
29. Hamrick, Y.M. and Weltner, W., Jr. *J. Chem. Phys.* **1981**, 74, 3584.
30. Jaycox, M.E. *J. Mol. Spec.* **1985**, 113, 286.
31. Jaycox, M.E. *J. Mol. Struct.* **1987**, 157, 43.
32. Li, S.; Van Zee, R.J.; and Weltner, W., Jr. *J. Chem. Phys.* **1994**, 100, 7079.
33. Green, D.W.; Korfomacher, W.; and Gruen, D.M. *J. Chem. Physics*, **1973**, 58, 1, 404.
34. Shchukarev, S.A.; Semenov, G.A.; Frantseva, K.E. *Russian Journal of Inorganic Chemistry*. **1966**, 11, 2, 129.
35. Gatterer, A.; Junkes, J.; Salpeter, E.W.; and Rosen, B. *Molecular Spectra of Metallic Oxides*; Specola, Vaticana, **1957**.

36. Rao, V.R. and Premaswap, D. *Ind. J. Phys.* **1953**, 27, 399.
37. Brom, J.M., Jr.; Durham, C.H., Jr.; and Weltner, W., Jr. *J. Chem. Phys.* **1974**, 61, 3.
38. Li, S.; Van Zee, R.J.; and Weltner, W., Jr. *J. Chem. Phys.* **1997**, 106, 2055.
39. Ozin, G.A. and McCaffrey, J.G. *J. Phys. Chem.* **1984**, 88, 645.
40. Gershikov, A.G.; Spirdinov, V.P.; Prikhod'ko, A.YA.; and Erokhin, E.V. *High Temp. Sci.* **1981**, 14, 17.
41. Kohler, J.; Disselhorst, J.A.J.M.; Donckers, M.C.J.M.; Groenen, E.J.J.; Schmidt, J.; and Moerner, W.E. *Nature*. **1993**, 363, 242.
42. Fan, F-R. F. and Bard, A.J. *Science*. **1995**, 267, 871.
43. Burnett, K. *Science*. **1995**, 269, 182.
44. Hill, T.L. *Statistical Thermodynamics*. 2nd ed., Dover Publications, Inc., New York, **1986**.
45. Angus, S.; Armstrong, B.; De Reuck, K.M., *International Thermodynamic Tables of the Fluid State Vol. 3: Carbon Dioxide*, Pergamon Press, Oxford, **1976**.
46. Kordikowski, A.; Robertson, D.G.; Poliakoff, M.; DiNoia, T.D.; McHugh, M.; and Aguiar-Ricardo, A. *J. Phys. Chem. B*. **1997**, 101, 5853.
47. Pitzer, K.S. *Thermodynamics*. 3rd ed., McGraw-Hill, New York, **1995**.
- 48.. Serway, R.A. and Faughn, J.S. *College Physics*. Saunders College Publishing, Philadelphia, **1985**.
49. Weast, R.C. *CRC Handbook of Chemistry and Physics*. 1st Student Ed., CRC Press Inc., Boca Raton, **1990**.
50. Tatro, D.S., Ph.D. Dissertation, University of Florida, **1996**.

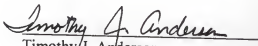
BIOGRAPHICAL SKETCH

Troy Daniel Halvorsen was born on February 20, 1968, in Belvidere Illinois, to Dan and Susan Halvorsen. He was graduated from Southeast High School in Springfield, Illinois in June 1986. He was graduated from Illinois State University in Normal, Illinois in May 1990 with a Bachelor of Science in Chemistry. He completed his Master's degree in 1993, under the guidance of Professor Cheryl Stevenson, also at Illinois State. Since August of 1993 he has attended Graduate School at the University of Florida where he has pursued the degree of Doctorate of Philosophy in physical chemistry. He enjoys spending time with friends and family, especially his wife, Kim, and daughter, Alana.

I certify that I have read this study and that in my opinion it conforms to the acceptable standards of scholarly presentation and is fully adequate, in scope and quality, as a dissertation for the degree of Doctor of Philosophy.


John R. Reynolds
Professor of Chemistry

I certify that I have read this study and that in my opinion it conforms to the acceptable standards of scholarly presentation and is fully adequate, in scope and quality, as a dissertation for the degree of Doctor of Philosophy.

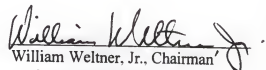

Timothy J. Anderson
Professor of Chemical Engineering
Sciences

This dissertation was submitted to the Graduate Faculty of the College of Liberal Arts and Sciences and to the Graduate School and was excepted in partial fulfillment of the requirements for the degree of Doctor of Philosophy.

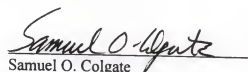
August 1998

Dean, Graduate School

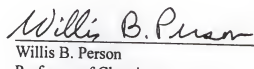
I certify that I have read this study and that in my opinion it conforms to the acceptable standards of scholarly presentation and is fully adequate, in scope and quality, as a dissertation for the degree of Doctor of Philosophy.


William Weltner, Jr., Chairman
Professor of Chemistry

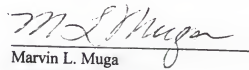
I certify that I have read this study and that in my opinion it conforms to the acceptable standards of scholarly presentation and is fully adequate, in scope and quality, as a dissertation for the degree of Doctor of Philosophy.


Samuel O. Colgate
Professor of Chemistry

I certify that I have read this study and that in my opinion it conforms to the acceptable standards of scholarly presentation and is fully adequate, in scope and quality, as a dissertation for the degree of Doctor of Philosophy.


Willis B. Person
Professor of Chemistry

I certify that I have read this study and that in my opinion it conforms to the acceptable standards of scholarly presentation and is fully adequate, in scope and quality, as a dissertation for the degree of Doctor of Philosophy.


Marvin L. Muga
Professor of Chemistry

LO 1780 1998

.H197

UNIVERSITY OF FLORIDA



3 1262 08555 0969